PHYSICAL REVIEW C **100**, 024003 (2019)

Three-body breakup in deuteron-deuteron collisions at 160 MeV including quasifree scattering

I. Ciepał,[1,*] G. Khatri,[2] K. Bodek,[3] A. Deltuva,[4] N. Kalantar-Nayestanaki,[5] St. Kistryn,[3] B. Kłos,[6] A. Kozela,[1] J. Kuboś,[1]
P. Kulessa,[1] A. Łobejko,[6] A. Magiera,[3] J. Messchendorp,[5] I. Mazumdar,[7] W. Parol,[1] R. Ramazani-Sharifabadi,[5,8]
D. Rozpędzik,[3] I. Skwira-Chalot,[9] E. Stephan,[6] A. Wilczek,[6] B. Włoch,[1] A. Wrońska,[3] and J. Zejma[3]
[1]*Institute of Nuclear Physics, PAS, PL-31342 Kraków, Poland*
[2]*Department of Physics and Astronomy, Northwestern University, Evanston, Illinois 60208, USA*
[3]*Institute of Physics, Jagiellonian University, PL-30348 Kraków, Poland*
[4]*Institute of Theoretical Physics and Astronomy, Vilnius University, Vilnius, Lithuania*
[5]*KVI-CART, University of Groningen, NL-9747 AA Groningen, The Netherlands*
[6]*Institute of Physics, University of Silesia, PL-41500 Chorzów, Poland*
[7]*Tata Institute of Fundamental Research, Mumbai 400 005, India*
[8]*Department of Physics, University of Tehran, Tehran, Iran*
[9]*Faculty of Physics University of Warsaw, PL-02093 Warsaw, Poland*

(Received 18 May 2019; published 28 August 2019)

A set of differential cross section of the three-body $^2\mathrm{H}(d,dp)n$ breakup reaction at 160-MeV deuteron beam energy is presented for 147 configurations covering a wide kinematical region around quasifree scattering. The experiment was performed at KVI in Groningen, the Netherlands, using the BINA detector. The cross-section data have been normalized to the $^2\mathrm{H}(d,d)^2\mathrm{H}$ elastic-scattering cross section. The data are compared to the results of recent single-scattering approximation (SSA) calculations for three-cluster breakup in deuteron-deuteron collisions. This comparison shows that SSA provides the correct order of magnitude of the cross sections. The studied energy is probably too low to meet the SSA assumptions which prevents better accuracy of the description.

DOI: 10.1103/PhysRevC.100.024003

I. INTRODUCTION

After a long quest lasting several decades for three-nucleon force (3NF) effects in three-nucleon systems (3N) at intermediate energies, the attention is nowadays directed to heavier systems composed of four nucleons (4N).

In the past decades, various final states of *N-d* and *d-N* scattering were under extensive investigations delivering high-precision data for elastic-scattering, breakup, and radiative capture reactions covering wide ranges of energy and phase space [1–3]. Together with rigorous Faddeev calculations for the 3N system the data provide a sensitive tool to study dynamics of nuclear systems. Among all the reactions studied, the breakup leading to a final state with three free particles offers the richest phase space with continuum of the final states and is the leading channel at intermediate energies. A large amount of possible kinematic configurations makes possible a systematic study of various dynamical effects like 3NF, Coulomb force between protons, or relativistic effects, which manifest themselves locally with different strength. These features make the breakup reaction a very sensitive and simultaneously strict tool for validation of the theoretical models.

The present-day models of nucleon-nucleon (NN) forces are based on the meson-exchange theory, which stems from Yukawa's idea [4]. The new generation NN potentials like Argonne V18 (AV18) [5], CD Bonn (CDB) [6], and Nijmegen I and II [7] reproduce the NN data with extremely high precision, expressed by χ^2 per degree of freedom very close to 1. These so-called realistic NN forces are used in 3N Faddeev equations [8] together with current models of 3NF like Urbana IX [9], Tucson-Melbourne [10], and a coupled-channels potential CD Bonn + Δ [11,12] with a Δ-isobar degree of freedom, delivering an exact solution of the 3N-scattering problem. These studies are complemented by calculations based on chiral perturbation theory (ChPT) [13,14], which are expected to provide in the future a consistent description of 2N, 3N (4N, etc.) forces.

While the NN potentials supplemented with the 3NF models give a better agreement between the proton-deuteron cross-section data and the calculations [15–18], there exist many problems in the spin observables [19,20]. This leads to a conclusion that the spin part of 3NF is still not under control in the theoretical models. It seems that at intermediate and higher energies the inclusion of 3N forces is necessary [2,3,15,16,18–21] but available models are not sufficient. At lower energies persistent discrepancies exist such as the A_y puzzle or the space-star anomaly [1].

The 4N systems constitute another large and important basis for studies of the 3N forces. Naively, one can expect the 3NF effects to be larger in the 4N system due to the fact that the number of 3N combinations with respect to 2N combinations gets larger with increasing number of nucleons.

---

[*] izabela.ciepal@ifj.edu.pl

However, due to expected short range of 3NF, for large nuclei, the saturation of 3NF effects sets in very quickly. The 4N systems are very suitable to study the 3NF dependence on spin and isospin in the low-energy regime due to the existence of numerous resonance states of different spin and isospin structure. Moreover, they reveal extra sensitivity toward NN force models and can help to understand the isospin symmetry of NN P waves [22,23]. This, in turn, is important for solving the deuteron analyzing power puzzle or the space-star anomaly [1]. The 4N systems are also suitable to test various nuclear potentials in an isospin-dependent way [24,25]. This makes the experimental studies attractive; however, the theoretical treatment of 4N scattering at medium energies (well above the breakup threshold) is much more complicated and challenging than for 3N systems. The developments in the calculations where four nucleons are involved are mainly due to the work of three groups: Pisa [22,26], Grenoble-Strasbourg [23,27], and Lisbon-Vilnius [12,28,29]. Only the Lisbon-Vilnius group calculates observables for multichannel reactions above the breakup threshold and with the Coulomb force included. They use the momentum space equations of Alt, Grassberger, and Sandhas (AGS) [30] for the transition operators in contrary to the two other groups which use the coordinate-space representation.

Recently, the calculations were extended for higher energies, above the four-cluster breakup threshold, up to an energy of 35 MeV. The following models were utilized in the calculations: CD Bonn [6] and Argonne V18 [5] potentials, the inside-nonlocal outside-Yukawapotential by Doleschall [31], potential derived from ChPT at next-to-next-to-next-to-leading order [13], and the two-baryon coupled-channels potential CD Bonn + Δ [11]. The last model yields effective three- and four-nucleon forces [12], but their effect is of moderate size at most. The sensitivity to the force model in the energy range studied reached 30% in the cross-section minimum. The predictions have been made for observables in p-^{3}He [32], p-^{3}H, and n-^{3}He [28] elastic-scattering and transfer reactions. Recent progress in calculations for the $d+d$ system is presented in Refs. [29,33,34].

The first estimate calculations for the $d+d$ system at higher energies are currently feasible and were performed in the so-called single-scattering approximation (SSA) for the three-cluster breakup and elastic scattering [33]. In this approximation, instead of solving the full AGS equations, the 4N operators are expanded in Neumann series in terms of 3N transition operators and only the first-order contribution is retained. This simplification could be expected to give reasonable predictions only near quasi-free-scattering (QFS) kinematics and with high-enough relative n-d and n–p energies that imply relatively high beam energies.

Two types of calculations were performed. The first one, the so-called one-term (1t) SSA, refers to a situation in which the target deuteron breaks due to its proton interaction with the deuteron beam. In this case the differential cross section is peaked at the neutron spectator energy $E_n = 0$. The second one, the so-called four-term (4t) SSA, on top of the one-term SSA contains other three contributions, one of them corresponding to the case in which not the target proton but the neutron interacts with the beam deuteron. Two further contributions arise from exchanging the target and beam deuterons, i.e., they correspond to the breakup of the beam deuteron. Since the Coulomb force and interaction in two of three pairs of three final clusters d, p, and n are neglected, the relative energy between those clusters should be high enough to reduce the effects of the final-state interaction. An agreement between one-term and four-term calculations indicates that the one-term reaction mechanism dominates in the scattering. The disagreement is a hint of a more complicated reaction mechanism and behavior beyond SSA.

To investigate the reliability of the SSA calculations, a similar approximation was applied to $p+d$ breakup. The SSA calculations were compared with the exact ones. The total $p+d$ breakup cross section calculated precisely is lower than the one obtained in SSA by 30% at 95 MeV and by 20% at 200 MeV. The authors of Ref. [33] conclude that the SSA should provide correct orders of magnitude for total and differential cross sections for $d+d$ and $p+d$ breakup (near quasifree region) and elastic scattering.

Since n-^{3}He experiments are difficult, the p-^{3}He and $d+d$ reactions dominate in measurement for the 4N system. The theoretical calculations for the p-^{3}He system are the simplest, since only elastic and breakup channels exist. On the other hand, the most serious complication arises from the Coulomb interaction between protons, which is treated using the method of screening and renormalization [32]. The database for the 4N systems consist of few measurements for the elastic [35–38], breakup [39–44], and transfer channels [45,46]. In the breakup sector the existing data are usually limited to low energies and only very few selected configurations. The new-generation data covering large phase space were measured at Kernfysisch Versneller Instituut (KVI) at 130 [38,47] and 160 MeV (this paper). The data evaluation was focused on QFS, with neutron acting as a spectator. The breakup analyzing power data for the ^{2}H$(d,dp)n$ at 130 MeV were compared with the elastic d-p scattering [38,47]. Recently, the data have been also compared to the SSA calculations and large discrepancy of a factor 1000 was observed for differential cross section [33], indicating a need to revise both theory and data.

In this paper a rich set of the ^{2}H$(d,dp)n$ differential cross section near the QFS region at 160-MeV deuteron beam energy is presented. The data are compared with the SSA calculations.

II. EXPERIMENTAL TECHNIQUE

The experiment was carried out at KVI in Groningen, the Netherlands. The deuteron beam was provided by the superconducting cyclotron Accelerator Groningen ORsay at kinetic energy of 160 MeV and was impinging on a liquid deuterium target with the nominal thickness of 6.0 mm. Low beam current (about 5 pA) was used in order to keep the level of accidental coincidences as low as reasonable. The reaction products were detected using big instrument for nuclear polarization analysis (BINA) [48,49], designed to study few-body-scattering reactions at medium energies. The BINA setup allows us to register coincidences of two-charged particles in a nearly 4π solid angle, making possible studies of breakup

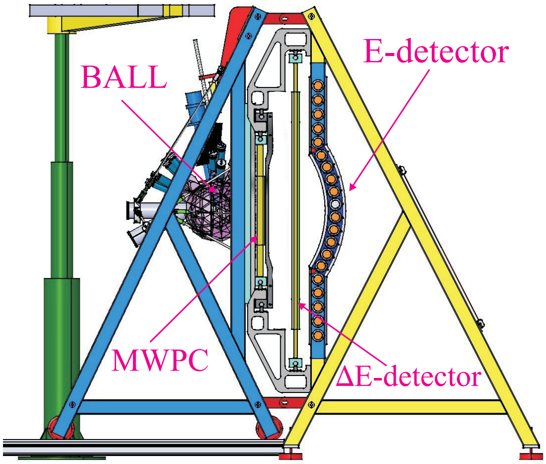

FIG. 1. A schematic view of the BINA detector.

and elastic-scattering reactions. The detector is divided into two main parts, the forward wall and the backward ball. A schematic view of the detection system is presented in Fig. 1.

A. Forward wall

The forward wall is composed of a three-plane multiwire proportional chamber (MWPC) and an array of an almost-square-shaped ΔE-E telescopes formed by two crossed layers of scintillator hodoscopes (vertically placed thin transmission-ΔE strips and horizontally placed thick stopping E bars). The forward wall covers polar angles θ in the range of 10°–35°. MWPC is used to determine the position of the passing particle. Taking into account the target and beam sizes, the accuracy of the angle reconstruction is 0.3° for θ and between 0.6° and 3° for φ. ΔE and E detectors are used for measuring the energies of the charged reaction products and facilitating particle identification. The energy resolution is about 2%. MWPC and the hodoscopes have a central hole to allow for the passage of beam particles to the beam dump.

For BINA the electronic, read-out, and data acquisition systems were adopted from its predecessor, the Small-Angle Large-Acceptance Detector (SALAD) [50]. The data were collected with various trigger conditions to selectively enhance coincidences from the studied reaction channels. The trigger conditions were based on hit multiplicities in left-side photomultipliers (PMTs) of the E detectors, right side PMTs of the E detectors, and PMTs of the ball. Three types of events were registered: wall-wall coincidences, wall-ball coincidences, and single-type events with at least one particle detected in the whole setup. The single-type events were strongly downscaled.

The results presented in this paper were obtained only on the basis of the data registered in the wall part of the detector.

III. DATA ANALYSIS

A. Reconstruction of particle trajectories

The tracks were built for each event, starting from hits in MWPC. Their correspondence with the ΔE and E detectors was checked in a track reconstruction procedure. Only events with the consistent information in all three detectors forming the track are likely to represent charged particles. In the analysis two kinds of tracks were considered to estimate the systematic errors related to the reconstruction: the so-called complete and weak tracks with the three and two responding MWPC planes, respectively. For complete tracks the reconstruction of angles has been improved, in comparison to the previous approaches [15,16,20], by taking into account also an active wire in the U plane. Consequently, the position resolution was improved by a factor of 1.5. In the case of the weak tracks based on information from the U plane, the position resolution in either horizontal or vertical direction worsen by a factor of 1.2 as compared to the tracks reconstructed on the basis of X and Y planes. Two classes of events were accepted for further analysis: single-track and two-track events. Tracks with missing MWPC or ΔE hits, but with a hit in E, were used to calculate detector efficiencies. Knowing the crossing point of the responding MWPC wires and distances between the target and the wire planes and assuming particle emission from the pointlike target, the polar (θ) and azimuthal (φ) scattering angles in the laboratory frame (LAB frame) were reconstructed.

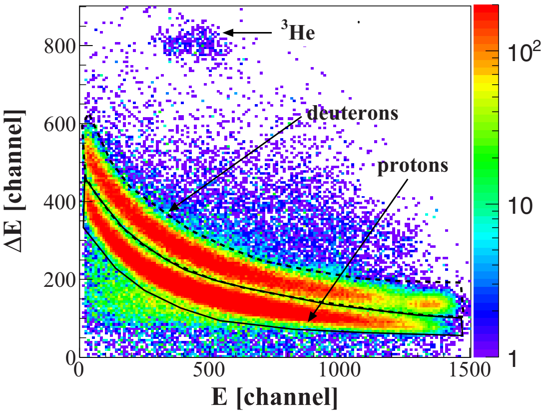

FIG. 2. Example of the ΔE-E identification spectrum drawn for one selected telescope. Proton and deuteron branches are well contained within the applied cuts which are depicted as black solid and dashed lines.

To calculate configurational efficiency of the E or ΔE detectors for coincident events, discussed further in Sec. III C 2, so-called *particular tracks* were reconstructed. Exactly two sets of X-Y-U hits in the three MWPC planes matching with a single E bar (or a single ΔE strip) were required.

B. Particle identification and energy calibration

In order to select the events of interest, proton-deuteron pairs from the breakup reaction, the ΔE-E particle identification (PID) technique was applied for each telescope. The protons and deuterons were selected by graphical cuts which define an arbitrary area (“banana” gate), wide enough to avoid significant losses of events. A sample identification spectrum is presented in Fig. 2.

After introducing PID into the analysis, the energy calibration was performed for each type of particles. In the case of the wall detector only the stopping E detector was calibrated. Each E bar is equipped with two PMTs on its two ends (left-PMT and right-PMT). When a charged particle hits the E detector, in an ideal situation both left and right PMTs respond, giving two pulse height values (C_L, C_R). The gains of PMTs were well matched, so the difference between C_L and C_R is mainly due to different light attenuation along the path in the scintillator. To perform the energy calibration for a given E bar, a nearly position independent C_{LR} variable was obtained as a geometric mean of C_L and C_R, i.e., $C_{LR} = \sqrt{C_L \times C_R}$. The exponential attenuation component cancels in the C_{LR} value. The central two E detectors were partially cut in the middle to accommodate beam line and in this case a sum of the two signals, i.e., $C_{LR} = C_L + C_R$ was used. To calibrate the detectors the positions of the peaks corresponding to protons originating from the d-p elastic-scattering process measured in dedicated runs with the energy degraders were used [51,52]. They were compared with the results of simulations taking into account energy losses of particles along their trajectory. In the first step a nonlinear function was fitted to the relation of the deposited energy versus pulse height. Such a nonlinear character (below 40 MeV) is caused by the quenching effect in the scintillating material (described with Birk's formula [53]). The calibration functions were obtained at each polar angle for left- and right-half sides of a given E detector. In the next step of the calibration the relation between the energy deposited by protons (or deuterons) in the E detector and their energy at the reaction point was found with the use of the dedicated GEANT4 (GEometry ANd Tracking) simulations of the energy losses in the BINA setup. Due to different scintillation light output for protons and deuterons, additional corrections were introduced to the deuteron calibration which were based on a well-known light output to energy deposit relations [54].

C. Detector efficiency

To extract the absolute values of the cross section, it is necessary to take into account the inefficiency of the detectors. In the case of the BINA setup, the largest inefficiency was related to the detection of particles in MWPC. During the experiment certain channels were malfunctioning or ceased to function at all ("dead" wires) decreasing the overall efficiency. Dependence of the MWPC efficiency on the energy deposition (E_{loss}) of a particle in this detector was observed and taken into account.

1. MWPC efficiency

In order to correct the number of registered proton-deuteron coincidences from the breakup reaction and elastically scattered deuterons, energy-loss-dependent efficiency maps were constructed, see also Ref. [46]. The detector acceptance was divided into bins in azimuthal and polar angles and efficiency was calculated for each cell with the use of the registered single particle events (protons and deuterons). Protons and deuterons were treated together to increase the precision of efficiency, and their energy loss E_{loss} were recalculated per unit distance according to the formula:

$$E_{\text{loss}} = Q^2 \frac{\alpha m}{T}, \tag{1}$$

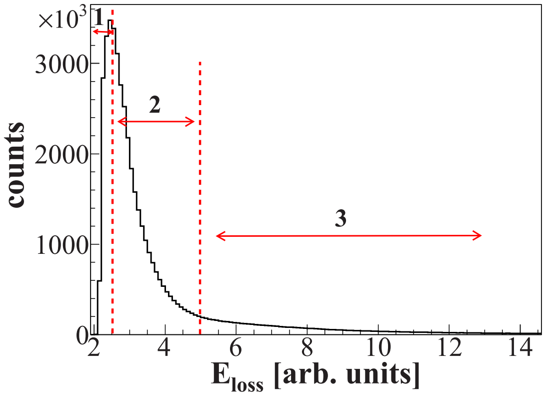

FIG. 3. The energy-loss E_{loss} distribution for the charged particles registered in the BINA setup. The three ranges in the E_{loss} variable in which the MWPC efficiency maps were obtained are depicted.

where Q is proton or deuteron charge, m is the mass of the particle, T is its kinetic energy, and α is an arbitrary constant factor. The efficiency maps were calculated for three ranges in the E_{loss} variable shown in Fig. 3. The active part of MWPC contains three planes: X, Y, and U, respectively with vertical, horizontal, and inclined by 45° wires. The position-sensitive efficiency of each plane was obtained using the information from the remaining two others [46,55] and combined with the information from the scintillator hodoscopes. The probability of registering a particle in a given MWPC plane, e.g., in the X plane, for a given angular bin (θ, φ) and E_{loss} range is given as:

$$\varepsilon_x(\theta, \varphi, E_{\text{loss}}) = \frac{N_{xyu}(\theta, \varphi, E_{\text{loss}})}{N_{yu}(\theta, \varphi, E_{\text{loss}})}, \tag{2}$$

where $N_{xyu}(\theta, \varphi, E_{\text{loss}})$ is the number of tracks registered in this angular bin with at least one wire hit in each of X, Y, and U planes, whereas $N_{yu}(\theta, \varphi, E_{\text{loss}})$ is the number of tracks with at least one wire hit in plane Y and one in plane U. The efficiencies of Y and U planes were calculated in a similar way. The overall MWPC efficiency for registration of tracks in three planes was obtained as a product of the particle registration probabilities in the individual planes:

$$\varepsilon_{xyu} = \varepsilon_x \varepsilon_y \varepsilon_u. \tag{3}$$

The MWPC efficiency presented in a form of θ, φ maps for the three E_{loss} ranges are presented in Fig. 4. The efficiency is the highest for the slowest particles which lose more energy in the detector so the signal is well above the applied thresholds. The difference in the total efficiency between the two maps is about 10%.

A similar map was created for the so-called weak tracks which allowed for one plane without hit. They were found to be much less sensitive to the energy loss of the particles. In this case the MWPC efficiency was calculated for the whole range of E_{loss} according to the formula:

$$\begin{aligned} \varepsilon_{xyu}^{\text{weak}} &= \varepsilon_{xyu} + \varepsilon_x \varepsilon_y (1 - \varepsilon_u) + \varepsilon_y \varepsilon_u (1 - \varepsilon_x) \\ &\quad + \varepsilon_u \varepsilon_x (1 - \varepsilon_y). \end{aligned} \tag{4}$$

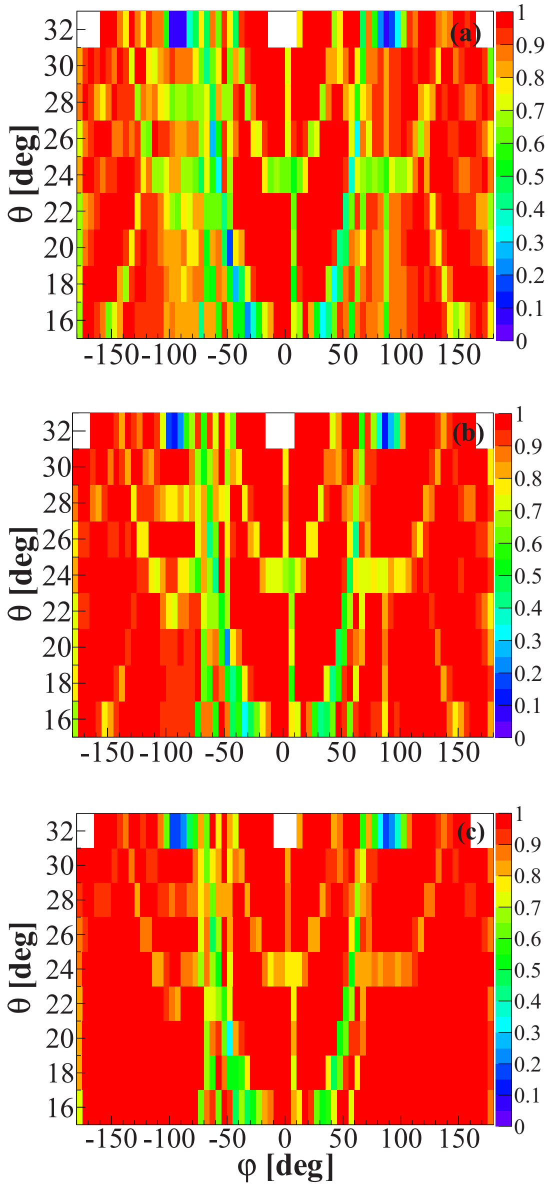

FIG. 4. The efficiency maps of MWPC for the three E_{loss} ranges defined in Fig. 3. The top map (a) refers to the lowest values of E_{loss} (the fastest particles, range 1), whereas the bottom one (c) is constructed for the highest E_{loss} (the slowest particles, range 3). The elliptic-like structures (light gray areas) correspond to "dead" or malfunctioning wires.

The resulting efficiency map is presented in Fig. 5. The total MWPC efficiency for weak tracks is about 98%.

Analogously to the case of MWPC, the efficiency map of the ΔE hodoscope was also constructed. The accumulated efficiency of this detector is around 95%. The efficiency of the E detector has been assumed to be 100%.

2. *Configurational efficiency*

Due to the fact that the events of interest are coincidences of two particles registered in E and ΔE detectors of a finite granulation, additional losses of acceptance have to be taken into account. The events with both particles registered in the same ΔE or E detector have to be rejected due to the lack of particle identification and/or unknown energy. Since the ΔE detector has two-times-finer granulation than the E detector (24 scintillators compared to 10), this effect is dominated by the E detector. Such inefficiency, in the following referred to as the *configurational efficiency*, is of geometrical origin and relevant only for coincidences. It is expected to be pronounced at small relative azimuthal angles of the proton-deuteron pair ($\varphi_{dp} \leqslant 80^\circ$).

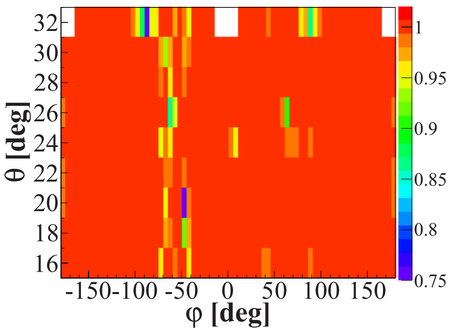

FIG. 5. The MWPC efficiency map obtained for weak tracks.

To establish the configurational efficiency the data collected with 160 MeV deuteron beam impinging on the proton target [56] were used. In the dp scattering only two channels are present: elastic scattering and *ppn* deuteron breakup, in contrast to the *dd* scattering [46], where four-body breakup and transfer channels also contribute. Therefore, any non-coplanar configuration of charged particles in dp-scattering data can be interpreted as the *ppn* breakup or, very unlikely, an accidental coincidence. The *ppn* channel has also advantage of low cross section at the ends of kinematical curves. The *dpn* channel, on the contrary, dominated by the quasifree process in which the events are usually gathered on the ends of the kinamatical curves (near detection thresholds) which is important in view of the discussion below. The configurational efficiency was calculated with the use of the *particular tracks* (defined in Sec. III A) for each geometrical configuration (θ_{p1}, θ_{p2}, φ_{12}) analyzed in this paper (see Sec. III F) with the same angular bins of $\Delta\theta = 2^\circ$, $\Delta\varphi_{12} = 10^\circ$ as applied in the analysis of the *dpn* breakup. The particular tracks include also events with one particle stopped in ΔE or with small energy deposit in E detector (below the threshold). In order to reject such events or minimize their impact, an upper limit was set on the energy deposited in ΔE. Based on the *ppn* breakup, angular information from MWPC (no PID available) and energy deposited in the ΔE detector, the efficiency was constructed as follows:

$$\varepsilon^{\mathrm{conf}}(\theta_{p1}, \theta_{p2}, \varphi_{12}) = \frac{N_{\mathrm{break}}(\theta_{p1}, \theta_{p2}, \varphi_{12})}{N_{ce}(\theta_{p1}, \theta_{p2}, \varphi_{12}) + N_{\mathrm{break}}(\theta_{p1}, \theta_{p2}, \varphi_{12})}, \quad (5)$$

where $N_{ce}(\theta_{p1}, \theta_{p2}, \varphi_{12})$ denotes the number of the p-p coincidences registered as the *particular tracks*, whereas $N_{\mathrm{break}}(\theta_{p1}, \theta_{p2}, \varphi_{12})$ denotes the number of the coincidences for the complete tracks. $N_{ce}(\theta_{p1}, \theta_{p2}, \varphi_{12})$ and $N_{\mathrm{break}}(\theta_{p1}, \theta_{p2}, \varphi_{12})$ represent experimental values obtained by

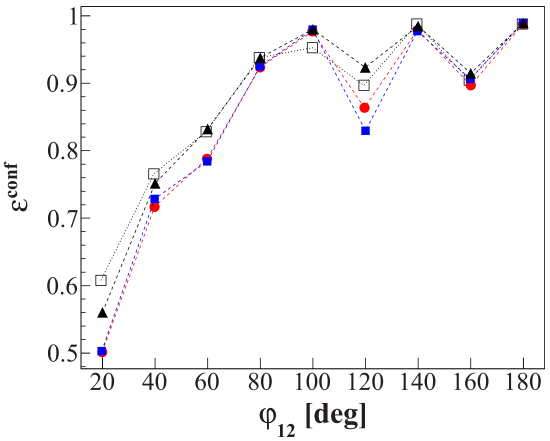

FIG. 6. Configurational efficiency ε^{conf} [see Eq. (7)] calculated on the basis of the ^{2}H$(p, pp)n$ data for $\theta_{p1} = 19^\circ$, $\theta_{p2} = 17^\circ$ in three cases: $+\varphi_{12}$ (blue squares), $-\varphi_{12}$ (black triangles), and $\pm\varphi_{12}$ (red circles). Empty squares represent results from the simulations for $\pm\varphi_{12}$. Lines connecting points are used to guide the eye.

integrating the events over the arclength S (see Sec. III F for definition of the S variable). In order to check our method, the data were analyzed for the kinematical configurations with $+\varphi_{12}$ (so-called normal configurations) and $-\varphi_{12}$ (so-called mirror configurations) separately and for $\pm\varphi_{12}$ (normal and mirror configurations treated together). As an example, the configurational efficiency for $\theta_{p1} = 19^\circ$, $\theta_{p2} = 17^\circ$ is presented in Fig. 6. In the case of $\varphi_{12} = 120^\circ$, values of ε^{conf} differ significantly between normal and mirror configurations.

The corrections should lead to the same results for the corresponding cross sections for the normal and mirror configurations, as follows from the parity conservation. In Fig. 7 the cross sections before (a) and after (b) the efficiency corrections are presented. The corrected cross sections are consistent within statistical errors. The corrections based on experimental data were compared to the GEANT4 simulations. In the simulations, the uniform three-body breakup phase-space distribution has been used, which is well justified in the case of narrow angular ranges applied in defining the configuration. The number of the breakup coincidences was counted and, simultaneously, a fraction of the breakup coincidences with two protons registered in the same E or ΔE detector was obtained. In Fig. 6 the ε^{conf} values resulting from the simulations are compared to the ones obtained on the basis of analysis of the particular tracks. The configurational efficiency calculated with the use of the simulations can be considered as purely geometrical factors of probability for double hits in a single E bar or a single ΔE strip. The data and the simulations agree qualitatively and usually the differences vary between 2 to 4% for the range of φ_{dp} above 120°, discussed in this paper. The statistical uncertainties are within 10%. These differences may lie in both simulations and the experimental data. On one hand, the simulations are rather simplified for not including data digitization and an ideal and realistic modeling of the detector geometry. On the other hand, the MWPC has its own configurational efficiency, which prevents the detection of two particles closer than the distance between two neighboring wires (2 mm) in the plane with horizontal wires. The further analysis relies on the corrections obtained directly from the experimental data.

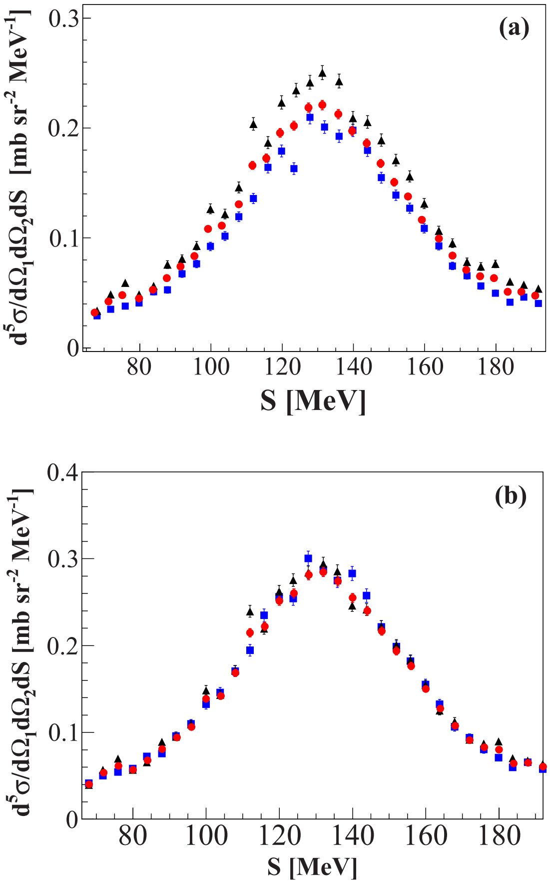

FIG. 7. Cross-section distributions for the ^{2}H$(p, pp)n$ breakup obtained for configuration $\theta_{p1} = 19^\circ$, $\theta_{p2} = 17^\circ$, $\varphi_{12} = 120^\circ$ before (a) and after (b) correction for configurational efficiency. Cross sections are presented for three cases for $+\varphi_{12}$ (blue squares), $-\varphi_{12}$ (black triangles), and $\pm\varphi_{12}$ (red circles).

In the range of φ_{dp} between 140° and 180°, which is being examined in this paper, practically only the efficiency losses due to double hits in the E detector matter. For the ΔE and MWPC detectors the configurational inefficiencies are negligible (below 1%).

D. Hadronic interactions

Additional losses of events took place due to hadronic interactions inside the scintillator material. They were treated as a background (see Sec. III F) together with events induced by charged particles on passive material of the detector setup. In order to correct the cross sections the losses were calculated for the protons and deuterons in the energy range of interest with the use of the GEANT4 framework [46]. The results of the calculations are presented in Fig. 8.

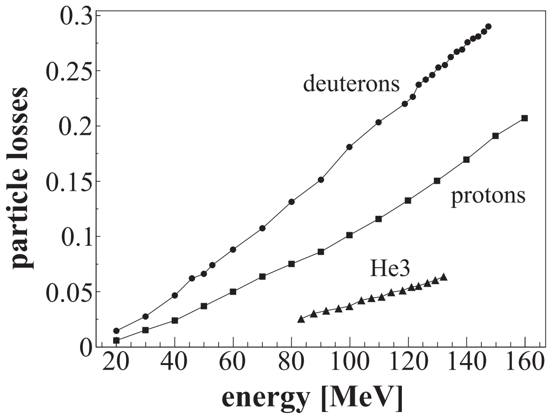

FIG. 8. Results of simulations of relative loss of events due to hadronic interactions of particles stopped in the plastic scintillator. The losses for protons, deuterons, and ^{3}He ions are presented as a function of initial energy at the target position.

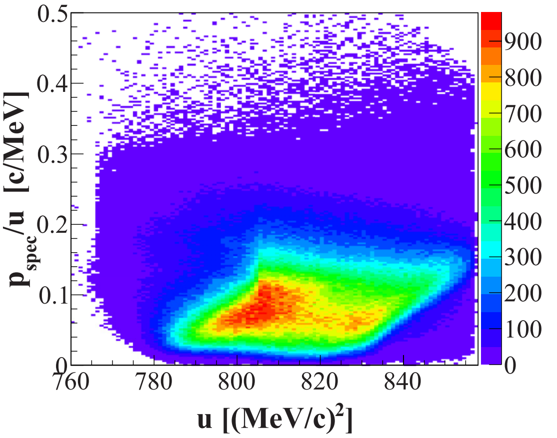

FIG. 9. The studied part of the phase space corresponding to θ_d, θ_p (15°–29°) and φ_{dp} (135°–185°) presented in terms of the p_{spec}/u versus the u variable.

E. Quasifree scattering

In QFS, a nucleon, or a nuclear fragment consisting of two or more nucleons, is knocked-out of the target nucleus in kinematic conditions close to the corresponding free scattering. In terms of the dynamics, QFS corresponds to a situation in which the interaction of the spectator with the incoming and outgoing particles is very weak or even absent. The deviation from free scattering will give information on the reaction mechanism and the structure of the nucleus.

The three-body QFS kinematics in the *dd* scattering can be realized in four ways: the deuteron projectile is scattered on the proton/neutron (*dp*/*n*-QFS) of the deuteron target or the proton/neutron (*p*/*nd*-QFS) of the beam deuteron is scattered on the deuteron target. In this paper only the *dp*/*n*-QFS is considered since in this case both outgoing charged particles are registered within the forward wall acceptance. The neutron from the deuteron target acts as a spectator which escapes practically untouched carrying the Fermi momentum possessed at the moment of the collision (neutron almost at rest in the LAB frame).

To learn about the *dpn* reaction dynamics in the QFS region one can investigate deviations from the elastic-scattering process and compare the data to calculations performed in the three-nucleon sector. Such studies were done at 130 MeV [38,47] near the QFS regime with the neutron acting as a spectator ("near" *dp*-QFS), i.e., $\vec{d} + d \rightarrow d + p + n_{\mathrm{spec}}$. The analyzing powers were directly compared to the $\vec{d}p$ elastic-scattering data and theory assuming free *dp* scattering. Contrary to the analysis at 130 MeV, in this paper the *dpn* breakup cross sections are presented in a much wider region around the QFS kinematics corresponding to θ_d and θ_p (15°–29°) and φ_{dp} (135°–185°). Due to the limitations of the MWPC acceptance at larger polar angles, the angular range was narrowed down to a maximum of 29° that partially removes some events originating from the "near" *dp*-QFS.

The QFS process is characterized by a two-body kinematics which implies a strong correlation in polar and azimuthal ($|\varphi_1 - \varphi_2| \approx 180°$) angles between the two final nucleons. Since the spectator emerges with its initial Fermi momentum, which in the deuteron is only around 80 MeV/*c*, it is clear that the QFS kinematics strongly prefers low neutron energies. In other words, when the momentum transfer (Mandelstam variable *u*) from a beam particle (deuteron) to a scattered one (proton) is large enough as compared to the spectator momentum (p_{spec}), the process could be considered quasifree scattering. The selected range of θ_d, θ_p (15°–29°) and φ_{dp} (135°–185°) corresponds to *u* between 760 and 860 (MeV/*c*)^2. The range of reconstructed momenta of neutrons in the studied part of the phase space is presented in Fig. 9 as a ratio of p_{spec} to *u* as a function of the *u* variable. With the use of the PLUTO event generator [57] in which the quasifree scattering is accomplished with a dedicated sampling model for the deuteron wave function [58], one can study separately the contributions from the *dpn* breakup (generated according to the phase space) and *dp*-QFS, see Fig. 10. Clearly, the region of low neutron momentum is dominated by the QFS, which proves the sensitivity of the selected angular range to the QFS kinematics. Since the SSA calculations provide only a rough estimation of three-body breakup cross sections in the QFS region, the experimental data are suitable to test that approach.

F. Breakup cross section

The geometry of a coincident proton-deuteron (*p*-*d*) pair is characterized by their polar angles θ_d and θ_p and relative azimuthal angle φ_{dp}. Momentum and energy conservation and the relation $\varphi_{dp} = |\varphi_d - \varphi_p|$ unambiguously define the kinematics of the ^{2}H(*d*, *dp*)*n* breakup which is described with five independent variables E_d, E_p, θ_d, θ_p, and φ_{dp}. The relation between energies E_p and E_d is represented with the kinematical curve, see Fig. 11. The energies E_p, E_d were transformed into two new variables defined in the E_p-E_d plane (see Fig. 11), with *D* denoting the distance of the (E_d, E_p) point from the kinematical curve for the pointlike geometry and *S* defining the arc-length along the kinematics with the starting point at the minimal E_p. In the analysis, the angular

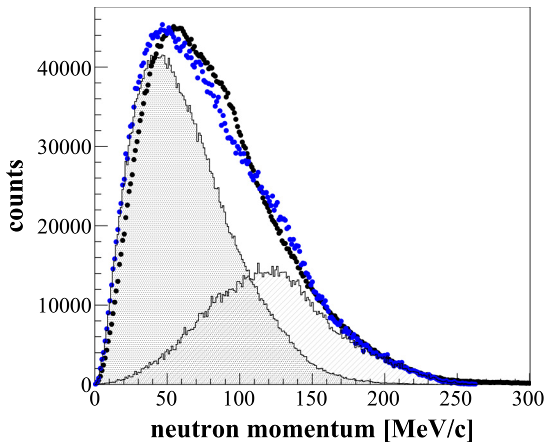

FIG. 10. Experimental distribution of the reconstructed neutron momentum (black points), obtained for the angular ranges of θ_d, θ_p (15°–29°) and φ_{dp} (135°–185°) compared to the PLUTO simulations for the *dpn* breakup (black hatched histogram) and *dp*-QFS (black dotted histogram) processes. The sum of simulated distributions is presented as a blue (gray) points. The simulated distributions were arbitrary normalized to the experimental one so that their sum reproduces the shape of the experimental histogram.

ranges for kinematic spectra were chosen as follows: $\Delta\theta_d = \Delta\theta_p = 2^\circ$ and $\Delta\varphi_{dp} = 10^\circ$ and are wide enough to reach a good statistical accuracy. The events in each bin of $\Delta S = 4$ MeV (see Fig. 11), corrected previously for efficiencies, were projected onto the D axis. The sample distribution in a function of the variable D is presented in the inset of Fig. 11. The breakup events are grouped in a prominent peak with only a very low background. Since the exact shape of the background is not known, as a first approximation, linear behavior was assumed. To calculate the cross section in a function of S, the Gauss function was fitted to the D distributions. To treat all configurations consistently, the integration limits in D variable were chosen at the values of D_a and D_b, see the inset of Fig. 11, corresponding to distances of -3σ and $+3\sigma$ from the maximum of the fitted peak.

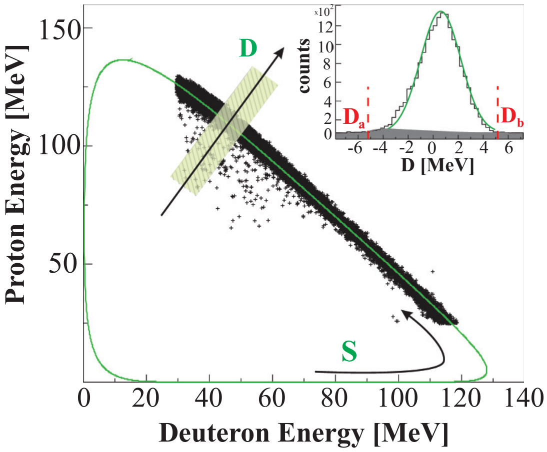

FIG. 11. E_p vs. E_d coincidence spectrum of the proton-deuteron pairs registered at $\theta_d = 20^\circ \pm 1^\circ$, $\theta_p = 18^\circ \pm 1^\circ$, $\varphi_{dp} = 160^\circ \pm 5^\circ$. The solid line shows a three-body kinematical curve calculated for the central values of the angular ranges. Variables arc-length S and distance from kinematics D are presented in a schematic way. The inset presents the D distribution of events belonging to one ΔS bin. The Gaussian distribution was fitted in the range of D corresponding to distances of $D_a = -3\sigma$ and $D_b = +3\sigma$ from the fitted peak position.

Measurements with an unpolarized beam and a detector with axial symmetry allows for integration of events over polar angles. The number of the proton-deuteron breakup coincidences $N_{\rm br}(S, \Omega_d, \Omega_p)$ registered at given angles $\Omega_d \equiv (\theta_d, \varphi_d)$ and $\Omega_p \equiv (\theta_p, \varphi_p = \varphi_d + \varphi_{dp})$ and in a S arc-length bin are given as follows:

$$\begin{aligned} &N_{\rm br}(S, \Omega_d, \Omega_p) \\ &\quad = \frac{d^5\sigma}{d\Omega_d d\Omega_p dS}(S, \theta_d, \theta_p, \varphi_{dp})\kappa\,\Delta\Omega_d\Delta\Omega_p\Delta S \\ &\qquad \times \varepsilon^d_{xyu}(\theta_d, \varphi_d, E_{\rm loss})\varepsilon^p_{xyu}(\theta_p, \varphi_p, E_{\rm loss}) \\ &\qquad \times \varepsilon^d_{\Delta E}(\theta_d, \varphi_d)\varepsilon^p_{\Delta E}(\theta_p, \varphi_p)\varepsilon^{\rm conf}(\theta_d, \theta_p, \varphi_{dp}), \end{aligned} \tag{6}$$

where $\frac{d^5\sigma}{d\Omega_d d\Omega_p dS}$ denotes differential cross section for the breakup reaction for a chosen angular configuration; solid angles are calculated as $\Delta\Omega_j = \Delta\theta_j\Delta\varphi_j \sin\theta_j$, $j = d, p$. ε^d_{xyu} and ε^p_{xyu} are the MWPC efficiencies, whereas $\varepsilon^d_{\Delta E}$ and $\varepsilon^p_{\Delta E}$ are ΔE efficiencies for registering deuteron and proton, respectively. $\varepsilon^{\rm conf}$ is the configurational efficiency (see Sec. III C 2). κ is the normalization factor defined in the next Sec. III G.

G. Cross-section normalization

The differential cross section for the ^{2}H$(d, dp)n$ breakup reaction was normalized to the known *d*-*d* elastic-scattering cross-section data. For that purpose the so-called scaling region characterized with very weak energy dependence of the cross section was used [46], which enables scaling of the measured elastic-scattering rate to the data at two closest energies (130 and 180 MeV) [37]. Such a relative normalization method ensures cancellation of factors related to the luminosity (i.e., the beam current, the thickness of the target) and to the electronic and readout dead times which otherwise can be a source of systematic uncertainties. The procedure of extracting the normalization factor κ, which corresponds to the luminosity integrated over the time of the data collection, is described in detail in Ref. [46]. For the data set presented in this paper, κ was established to be 48.4 ± 3.9 (syst.)$\times 10^6$ mb^{-1}. The statistical uncertainties are negligible.

H. Experimental uncertainties

The most serious sources of the systematic uncertainties which affect the breakup cross section are related to the PID method, the normalization procedure, a data averaging effect and the track reconstruction procedure. The systematic effects related to the normalization procedure were already described in Ref. [46], and here the systematic effects are discussed in the context of the breakup cross section.

Protons and deuterons were identified by defining graphical cuts enclosing the branches on the ΔE-E spectra. A finite precision in defining such cuts may lead to mixing of different particle types or cutting out a part of useful events. The systematic uncertainty associated with this process was estimated by repeating the analysis based on broad and narrow cuts of around 0.5σ of the original cut (σ is related to the width of ΔE distributions for a selected bin energy E). Based on this, the relative difference of the resulting cross sections was calculated. The typical uncertainty of the final breakup cross section related to PID do not exceed 5%.

The amount of background caused by the hadronic interactions (see Sec. III D) and to a lesser extent by the accidental coincidences was found low (see Fig. 11, inset), so the uncertainty related to background subtraction can be neglected. However, for a few configurations and certain S-bins the background contribution was significant and systematic effects connected to the background subtraction was found to be 2 to 5%.

For some sets of configurations significant systematic effects related to the calibration were observed. For these geometries the shape of the experimental kinematical curves differs from the theoretical one which influences the distributions of the cross section. In Fig. 12 an example for the $\theta_d = 28^\circ$, $\theta_p = 26^\circ$, $\varphi_{dp} = 180^\circ$ configuration is presented: Figures 12(a) and 12(b) show the original and scaled proton energy (so that to fit to the theoretical curve) distributions, respectively. The bottom figure [Fig. 12(c)] presents the resulting cross-section distributions. The size of the effect related to the events migration between different S bins was estimated to be 3 to 10%.

The experimental cross section for a given angular configuration (θ_d, θ_p, φ_{dp}) is evaluated by taking a finite bin width around these angles, i.e., $\theta_d \pm \frac{1}{2}\Delta\theta_d$, $\theta_p \pm \frac{1}{2}\Delta\theta_p$, and $\varphi_{dp} \pm \frac{1}{2}\Delta\varphi_{dp}$. The bin width is taken wide enough (here $\Delta\theta_d = \Delta\theta_p = 2^\circ$ and $\Delta\varphi_{dp} = 10^\circ$) to assure good statistical accuracy. On the other hand, the theoretical predictions, used for the comparison, were calculated at the central values of these angular bins. As explained in Ref. [18], the averaging of the calculations over the experimental bin width is quite crucial to validate theories in a reliable way. In order to estimate the associated systematics the analysis was performed with smaller bin sizes $\Delta\varphi_{dp} = 5^\circ$ and $\Delta\theta_p = \Delta\theta_d = 1^\circ$, see Fig. 13. The systematic error associated with this effect, in most cases, was found to be up to 5%.

Additional loss of events is related to the so-called crossover events [16]. Such events occur when particles penetrate from one stopping detector to the adjacent one and in this case events are lost due to distorted energy information. In this experiment, due to improper light tightness between E slabs, uncontrolled light leakage increased the crossovers. The systematic effects originating from the track reconstruction procedure and crossover losses were estimated based on the three data sets obtained separately for complete and weak tracks and with taking into account crossover events in the complete tracks reconstruction, see Secs. III A and III H. Such errors were calculated for each individual configuration. The deviations usually reach up to 7% and the maximum one is around 12%.

All the discussed above systematic errors are summarized in Table I. The total systematic uncertainty composed of systematic errors added in quadrature varies between 13 and 20%. The systematic error was estimated separately for each data point and the results are depicted as red bands in Fig. 14 and in Figs. 17–37 presented in the Appendix.

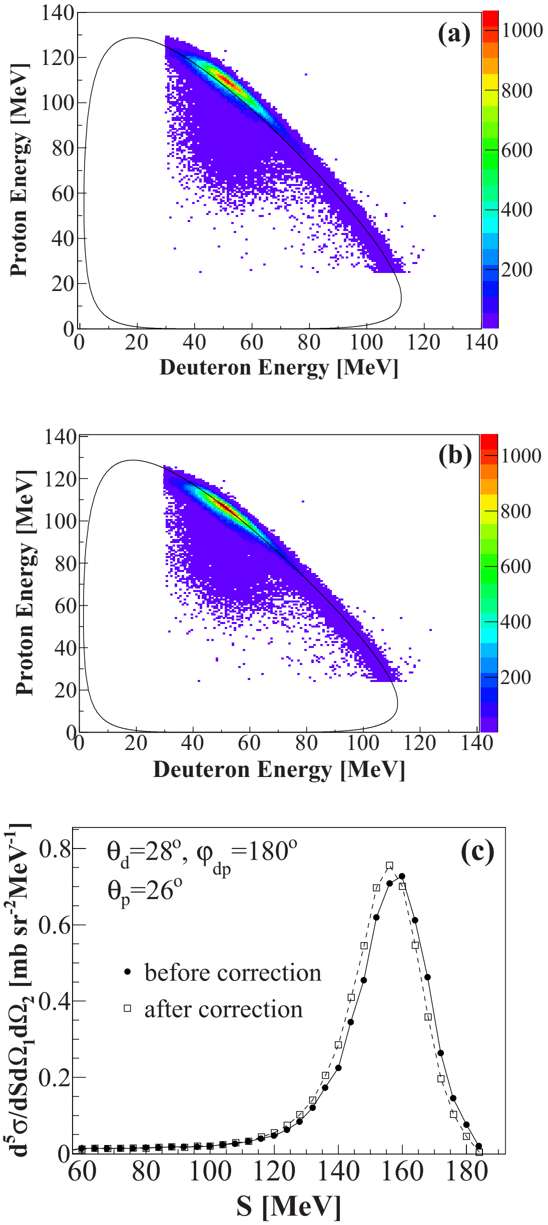

FIG. 12. E_p vs. E_d kinematical relation for the $\theta_d = 28^\circ$, $\theta_p = 26^\circ$, $\varphi_{dp} = 180^\circ$ configuration drawn together with the theoretical kinematical curve (a). The experimental kinematics scaled to the theoretical relation is presented in (b). The comparison of the cross-section distributions obtained for the above two cases (c) demonstrating the size of the systematic effect accounted for the calibration procedure. Lines connecting points are used to guide the eye.

IV. RESULTS AND COMPARISON TO THE SSA CALCULATIONS

The experimental cross-section data were obtained for 147 geometries of the proton-deuteron pairs from the breakup reaction in a wide kinematical region around the dp-QFS,

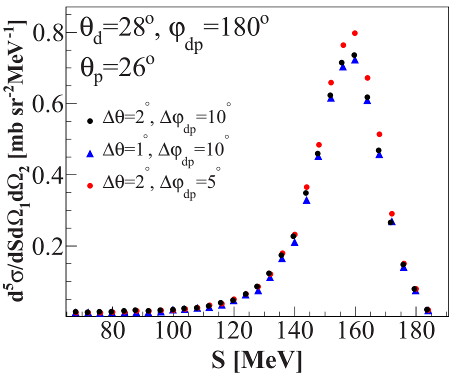

FIG. 13. Comparison of sample cross sections obtained with a regular bin size of $\Delta\varphi_{dp} = 10^\circ$ and $\Delta\theta_p = \Delta\theta_d = 2^\circ$ and smaller bin size of $\Delta\varphi_{dp} = 5^\circ$ and $\Delta\theta_p = \Delta\theta_d = 1^\circ$.

which corresponds to relative azimuthal angles φ_{dp}: 140°, 160°, and 180°. This part of the phase space does not include the full range of the QFS kinematics, as it was discussed in details in Sec. III E. Nonetheless, the data are still important for the validation of the SSA predictions around and beyond the QFS. Polar angles θ_d and θ_p were varied between 16° and 28° with the step of 2°. The theoretical predictions, used for the comparison with the experimental cross sections were calculated at the central values of the chosen angular bins. A sample cross-section distribution is presented in Fig. 14 together with the available SSA calculations, while the results for all individual configurations are collected in Figs. 17–37 in the Appendix.

The SSA calculations are expected to properly estimate the experimental data near QFS kinematics (i.e., with the neutron energy defined in the LAB frame $E_n \approx 0$) in the center-of-mass energies above 100 MeV. High-enough beam energy is necessary to ensure high relative energies for all pairs of nucleons. This, in turn, is important due to the fact that the final-state interactions are ignored in the calculations. With fixed beam energy these conditions can be met by considering relatively large scattering angles θ_d and θ_p. As it was stated in Ref. [33], SSA provides too-large cross sections and the discrepancy decreases with increasing beam energy. The total $p + d$ breakup cross section calculated in an exact way is lower than the one obtained in SSA by 30% at 95 MeV and by 20% at 200 MeV. In Nd systems, even with $E_n \approx 0$, SSA always gives higher values of the differential cross section than the exact calculations.

TABLE I. Sources and typical size of systematic effects. In cases of large spread of values, the maximal values are given in brackets.

Source of uncertainty	Size of the effect
PID	5%
Normalization	8% [46]
Reconstruction of angles	1%
Energy calibration	1% (max 10%)
Background subtraction	1% (max 5%)
Averaging effect	5%
Configurational efficiency	max 5% (for selected configurations)
Cross-section spread	7% (max 12%)
TOTAL	14% (20%)

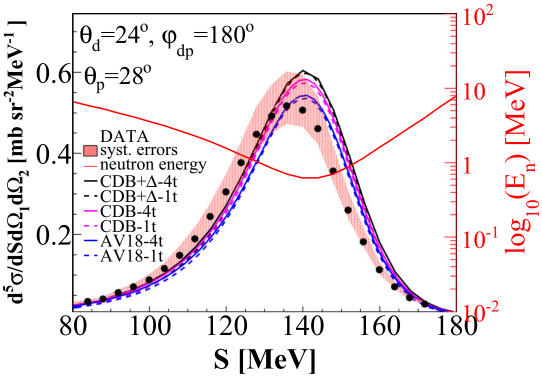

FIG. 14. Example of the differential breakup cross section for the angular configuration specified in the figure. The experimental points are marked with black dots. The systematic effects are depicted as a red band (gray band). Various lines represent the theoretical predictions calculated at the central values of the defined angular bins. The black lines refer to the SSA calculations based on the CD Bonn + Δ (CDB + Δ) potential: solid with four-term (4t) and dashed with one-term (1t). Solid and dashed magenta (light gray) and blue (dark gray) lines represent the similar set of the calculations but for the CD Bonn and AV18 potentials, respectively. The solid red line (upper line) present the dependence of the spectator neutron energy (E_n) on the S variable.

The data were sorted according to the relative energy E_{d-p} and the neutron energy in the LAB frame E_n, which in view of the above discussion are adequate for validating the SSA predictions. The quality of the agreement between the calculations and the experimental cross-section data was studied with the so-called A-deviation factor introduced in Ref. [59] and defined as follows:

$$A \equiv \frac{1}{N}\sum_{i=1}^{N}\frac{\left|\sigma_i^{\mathrm{exp}} - \sigma_i^{\mathrm{th}}\right|}{\sigma_i^{\mathrm{exp}} + \sigma_i^{\mathrm{th}}}, \tag{7}$$

where the sum runs over the number of data points in a given bin of E_n. In the previous analyses of the *ppn* data [15,16,18,20] the standardized χ^2 was used for the various exact calculations. The choice of the A factor instead of χ^2 is motivated by quite large discrepancies between the data and theories due to the approximate character of the calculations. The A factor has the advantage of its quite simple interpretation. Values of the A factor belong to the interval [0, 1], where zero means a perfect agreement between the data and calculations and with the deterioration of the agreement the A-factor approaches 1. For discrepancies small compared to cross-section values, the approximation $\sigma^{\mathrm{th}} \approx \sigma^{\mathrm{exp}}$ can be applied to the denominator and the A-factor value may be interpreted as half of the average relative distance between the experimental and theoretical cross sections.

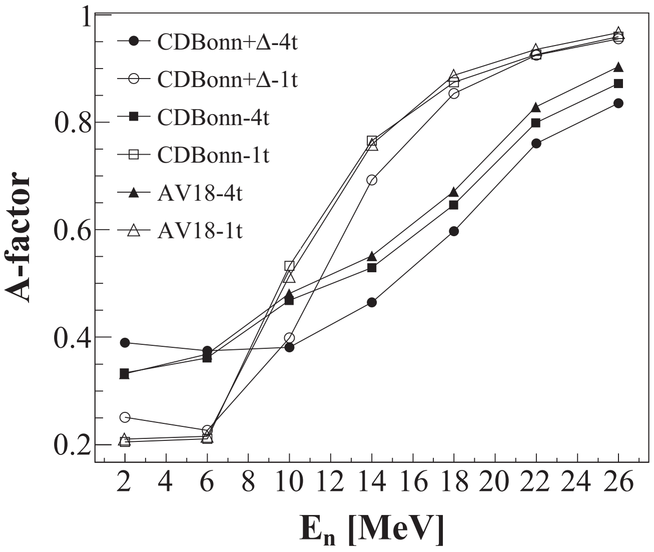

FIG. 15. Quality of the description of the cross-section data with various theoretical predictions (defined in the legend), expressed as dependence of the A factor on the neutron energy E_n. The bin size was chosen to be ±2 MeV. Lines connecting points are used to guide the eye.

In general one can conclude that at the lowest E_n the one-term calculations perform better than those with four terms, see Fig. 15. For $E_n < 10$ MeV the one-term calculations describe the data well. For higher E_n the agreement between the experimental and calculated cross sections deteriorates, but the four-term calculations stay closer to the data than the one-term ones. At highest available E_n the A factor evaluated for all calculations has values close or equal to 1, which means a failure of the theoretical description, as expected from the model assumptions [33].

In view of the above discussion on validity of SSA two-dimensional relations E_{d-p} vs. E_n were also investigated and are presented in Fig. 16, with the z axis representing the A factor for three sets of the calculations: CDB, CDB + Δ, and AV18 for the one- and four-term versions. Since the A factor does not account for statistical errors, the bins representing poor statistical accuracy are not shown. In the case of CDB + Δ the calculations were performed for three relative angles (140°, 160°, and 180°), therefore much more data points contribute, as seen in Figs. 16(c) and 16(d). For CDB and AV18 the theoretical calculations are available only at 180°.

The one-term predictions better describe the data for $E_n <$ 10, with the exception of combination of $E_n < 5$ MeV and $E_{d-p} > 40$ MeV, as seen in Fig. 16, where also four-term predictions are in agreement with the data. For $E_n < 2$ MeV, CDB and AV18 perform better than CDB + Δ.

The predicted 3NF effects in the QFS regions are small and having the approximate SSA calculations, no solid conclusions can be drawn about the interaction models. The SSA provides correct magnitude of the cross-section data; however, it seems that the deuteron beam energy of 160 MeV is still too low for SSA to provide more accurate results.

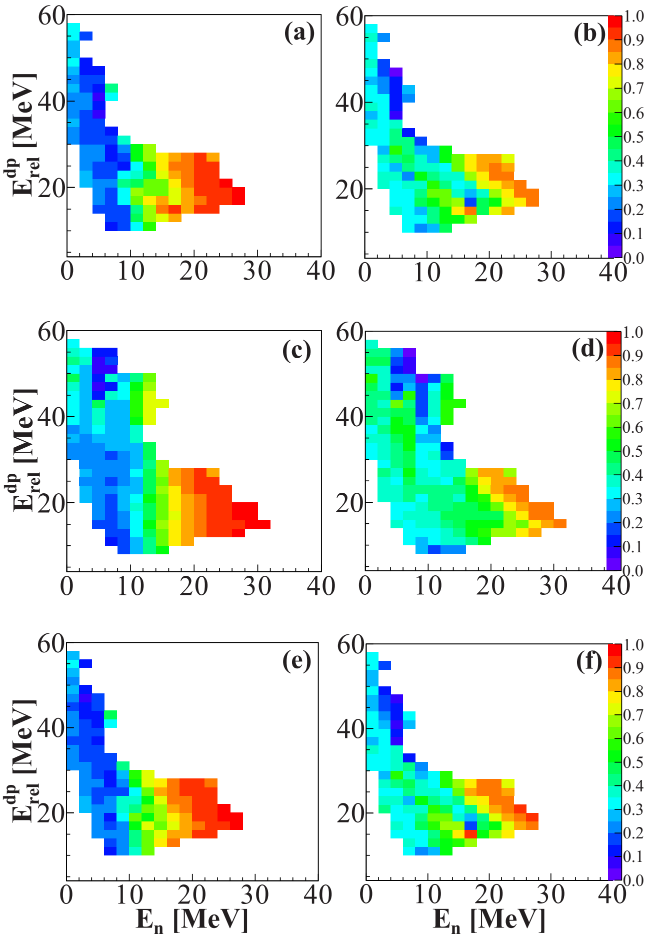

FIG. 16. Quality of the description in terms of the A factor given by SSA calculations with various potentials: CDB [(a) and (b)], CDB + Δ [(c) and (d)], and AV18 [(e) and (f)]. Left and right columns correspond to one- and four-term calculations, respectively.

V. SUMMARY AND OUTLOOK

The differential cross-section distributions for the three-body ^{2}H(d,dp)n breakup reaction have been obtained for 147 proton-deuteron geometries at 160-MeV deuteron beam energy. The analyzed part of the phase space covers a wide kinematical region around the dp-QFS and only partially includes the "near" dp-QFS. Despite these limitations, the obtained set of cross sections is still valuable for validating the recent 4N calculations. The cross sections have been compared to the calculations based on the single-scattering approximation for 4N systems at higher energies [33]. The system dynamics is modeled with AV18, CD Bonn, and CD Bonn + Δ potentials. The calculations are still not exact, but they provide a correct order of magnitude for the cross section close to the QFS region. In this region the SSA cross sections are usually higher than the experimental ones, roughly by a factor of 2 or 3, with the exception of a very limited region in a E_{d-p} vs. E_n plane, where the description of the data is satisfactory.

From the SSA calculations one could expect much better agreement between experimental and theoretical cross section at the lowest neutron spectator energies, but this picture may be disrupted due to too-low beam energy and not negligible final-state interactions.

The data measured at KVI at the deuteron beam energy of 130 MeV seem not to confirm the SSA results for the cross section [33,38,47]. So far the data were only published for one sample configuration ($\theta_d = 15^\circ$, $\theta_p = 15^\circ$, $\varphi_{dp} = 180^\circ$) [60].

The development of models involving 4N systems is ongoing, though exact numerical calculations for breakup amplitudes are still distant in time given the complexity of the problem. Current experimental efforts are focused on further development of the 4N database, which is very poor especially for the breakup channels. In particular, an emphasis is placed on investigations of proton-^{3}He scattering [61,62] since this system is the simplest one where the 3NFs in the channels of total isospin $T = 3/2$ can be studied [63]. Such isospin dependence studies of 3NFs are crucial for understanding of nuclear systems with larger isospin asymmetry like neutron-rich nuclei, neutron matter, and neutron stars [64,65].

ACKNOWLEDGMENTS

This work was supported by the Polish National Science Center under Grants No. 2012/05/E/ST2/02313 (2013–2016) and No. 2016/21/D/ST2/01173 (2017–2020) and by the European Commission within the Seventh Framework Programme through IA-ENSAR (Contract No. RII3-CT-2010-262010). A.D. acknowledges the support by the Alexander von Humboldt Foundation under Grant No. LTU-1185721-HFST-E.

APPENDIX: BREAKUP CROSS-SECTION DISTRIBUTIONS FOR INDIVIDUAL CONFIGURATIONS

This Appendix contains the cross sections of the three-body ^{2}H$(d, dp)n$ reaction at 160 MeV. The results, presented in Figs. 17–37, were obtained for the deuteron-proton coincidences registered at given θ_1, θ_2, and φ_{dp} angles, with the ranges of $\Delta\theta_d = \Delta\theta_p = 2^\circ$ and $\Delta\varphi_{dp} = 10^\circ$. The results are compared with a set of theoretical predictions, which are presented in the figures as color lines listed in the included legend. The experimental results and theoretical calculations are presented as a function of the arc-length S along the kinematical curve. In the figures the error bars represent the statistical uncertainties, whereas the systematic point-to-point errors are depicted as red (gray) bands.

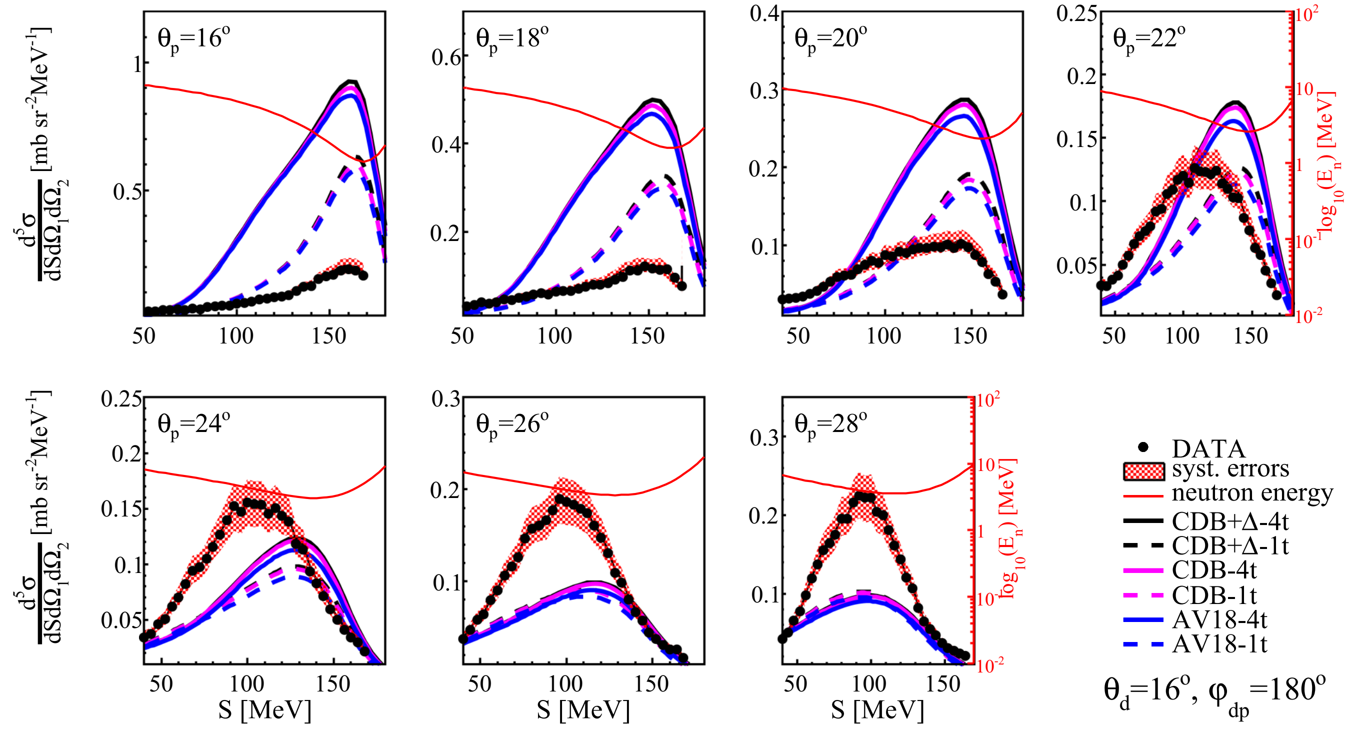

FIG. 17. Differential cross section distributions for the ^{2}H$(d, dp)n$ reaction obtained for the set of kinematic configurations characterized by $\theta_d = 16^\circ$, $\varphi_{dp} = 180^\circ$, and θ_p as specified in the panels. The dashed lines represent the one-term (1t) and solid lines four-term (4t) calculations based on pure CD Bonn (magenta/light gray), Argonne V18 (blue/dark gray), and CD Bonn + Δ (black) potentials, as described in the legend. The red (upper gray) line and the scale on the right-hand side present the dependence of the spectator neutron energy (E_n) on the S variable.

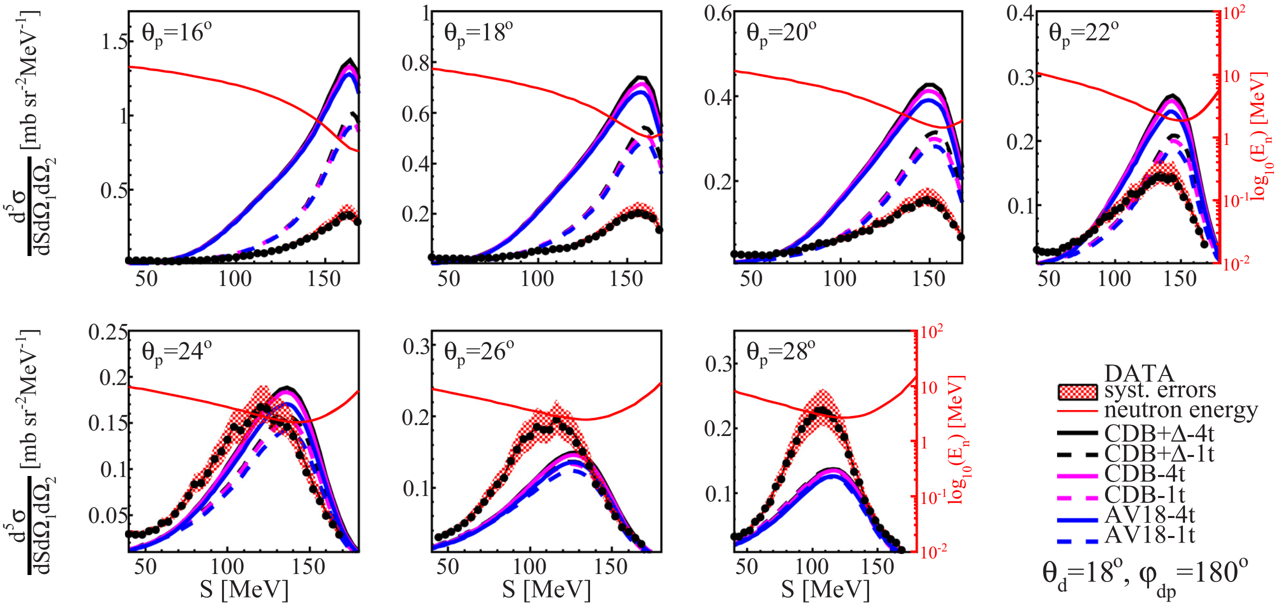

FIG. 18. Same as Fig. 17 but for $\theta_d = 18^\circ$.

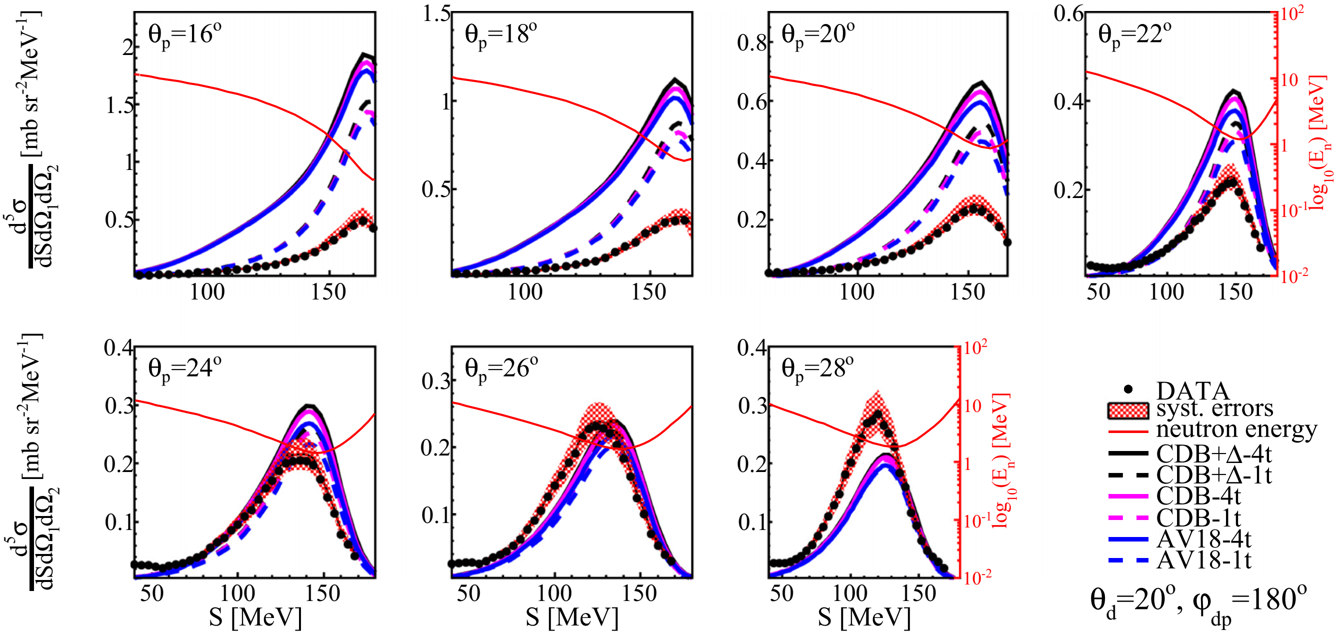

FIG. 19. Same as Fig. 17 but for $\theta_d = 20^\circ$.

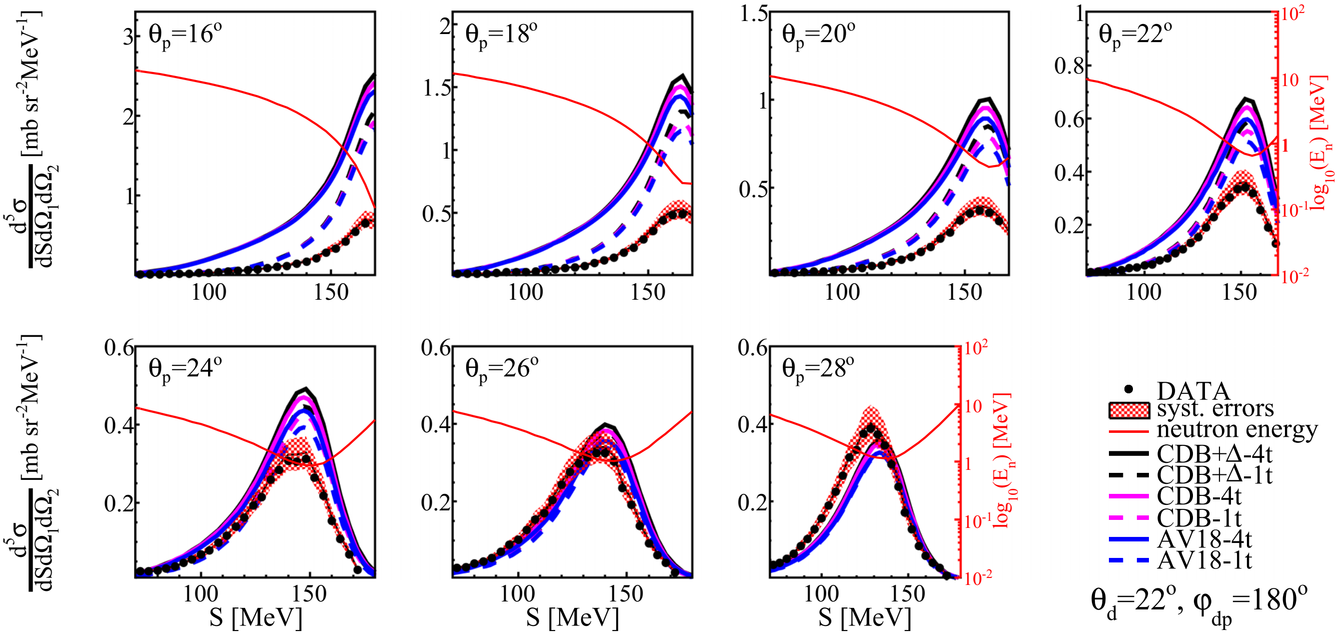

FIG. 20. Same as Fig. 17 but for $\theta_d = 22^\circ$.

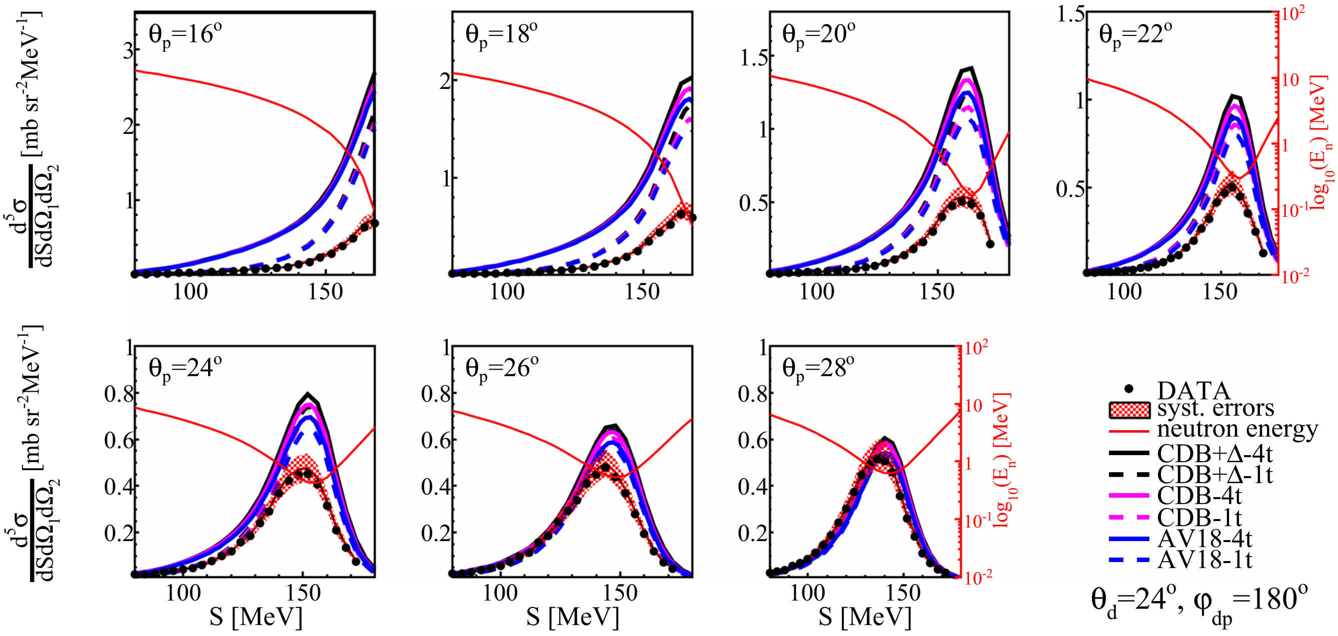

FIG. 21. Same as Fig. 17 but for $\theta_d = 24^\circ$.

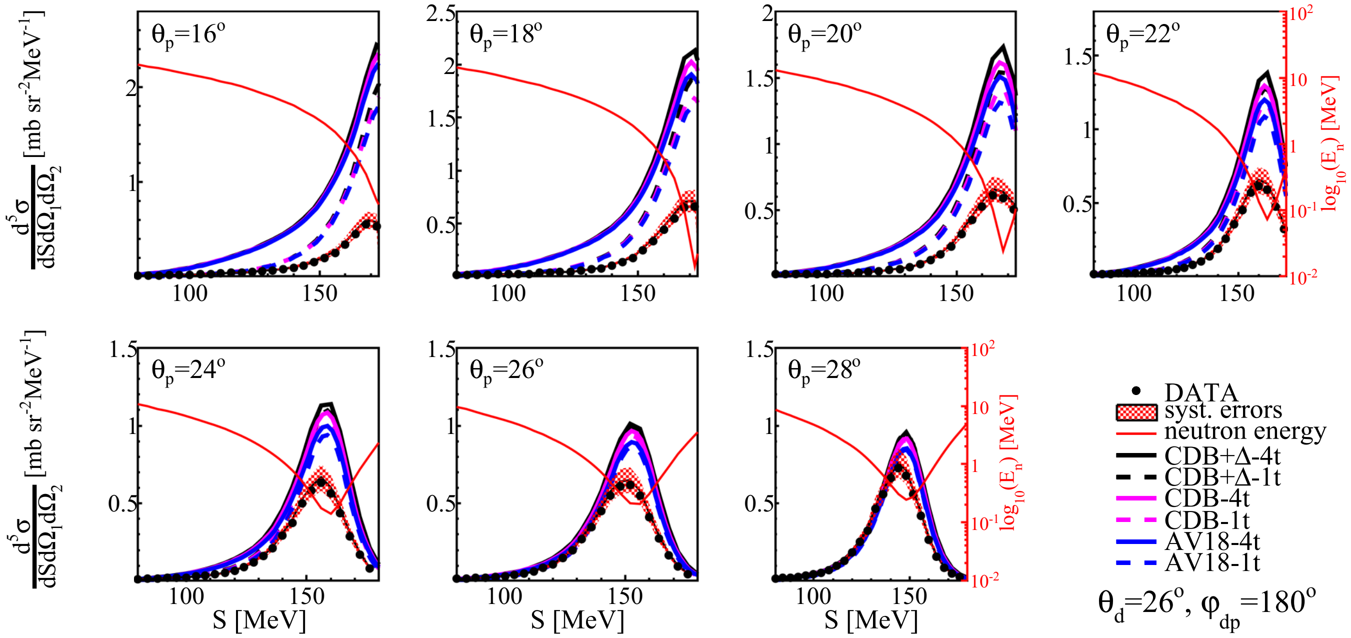

FIG. 22. Same as Fig. 17 but for $\theta_d = 26°$.

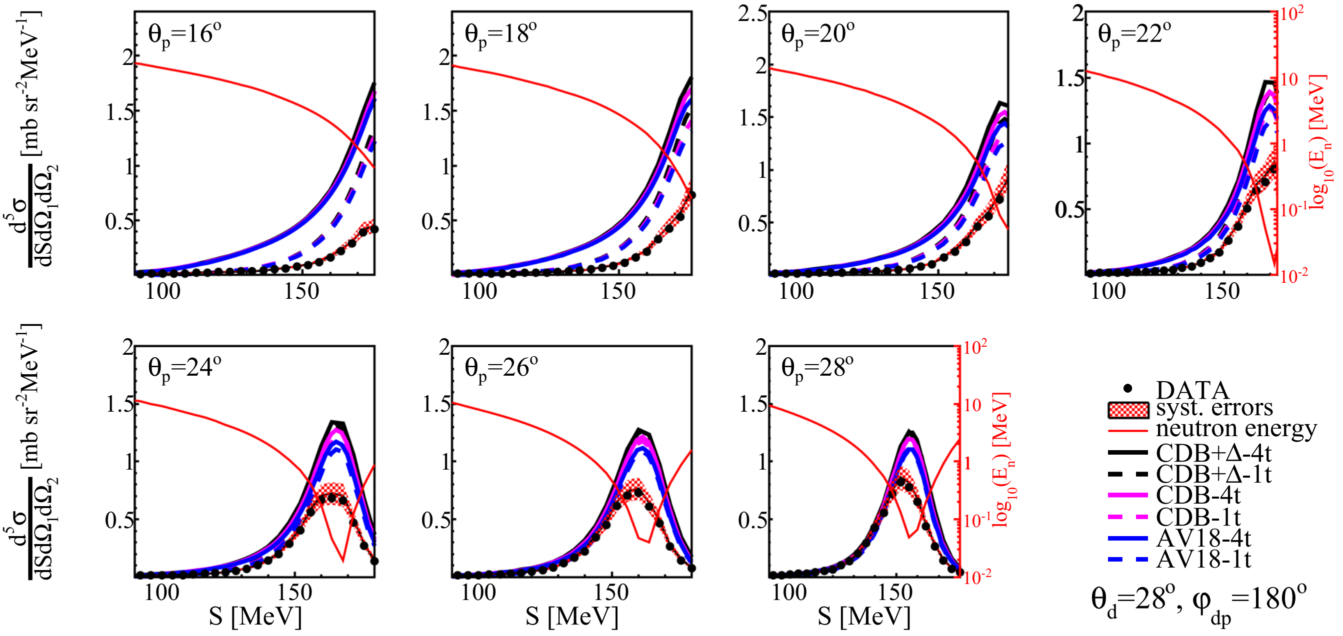

FIG. 23. Same as Fig. 17 but for $\theta_d = 28°$.

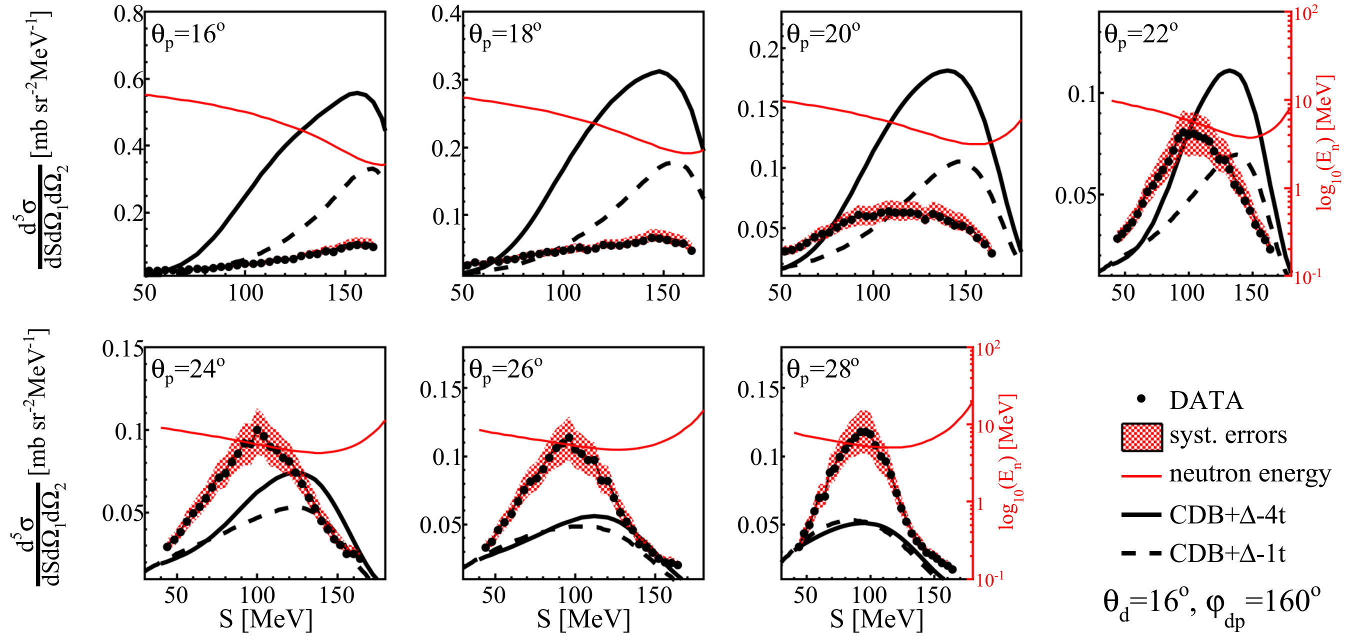

FIG. 24. Differential cross-section distributions for the ^{2}H(d, dp)n reaction obtained for the set of kinematic configurations characterized by $\theta_d = 16^\circ$, $\varphi_{dp} = 160^\circ$, and θ_p as specified in the panels. The dashed black lines represent the one-term (1t) and solid black lines four-term (4t) calculations based on the CD Bonn + Δ potential, as described in the legend. The red (upper gray) line and the scale on the right-hand side present the dependence of the spectator neutron energy (E_n) on the S variable.

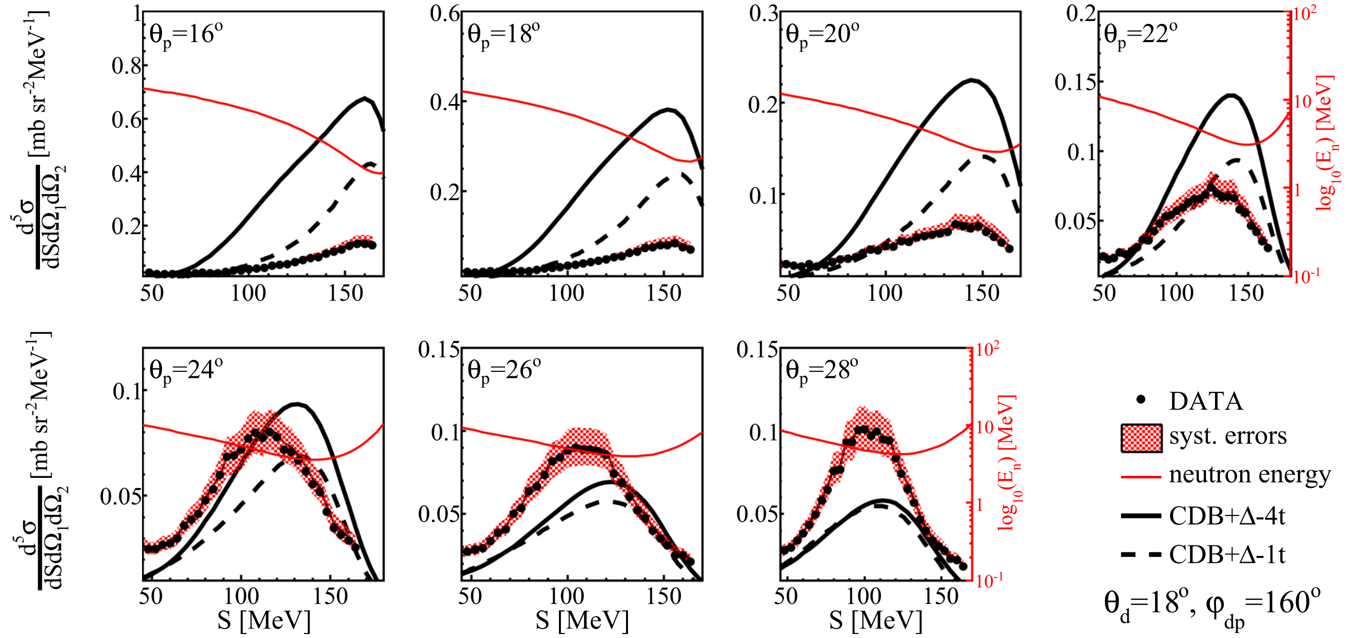

FIG. 25. Same as Fig. 24 but for $\theta_d = 18^\circ$.

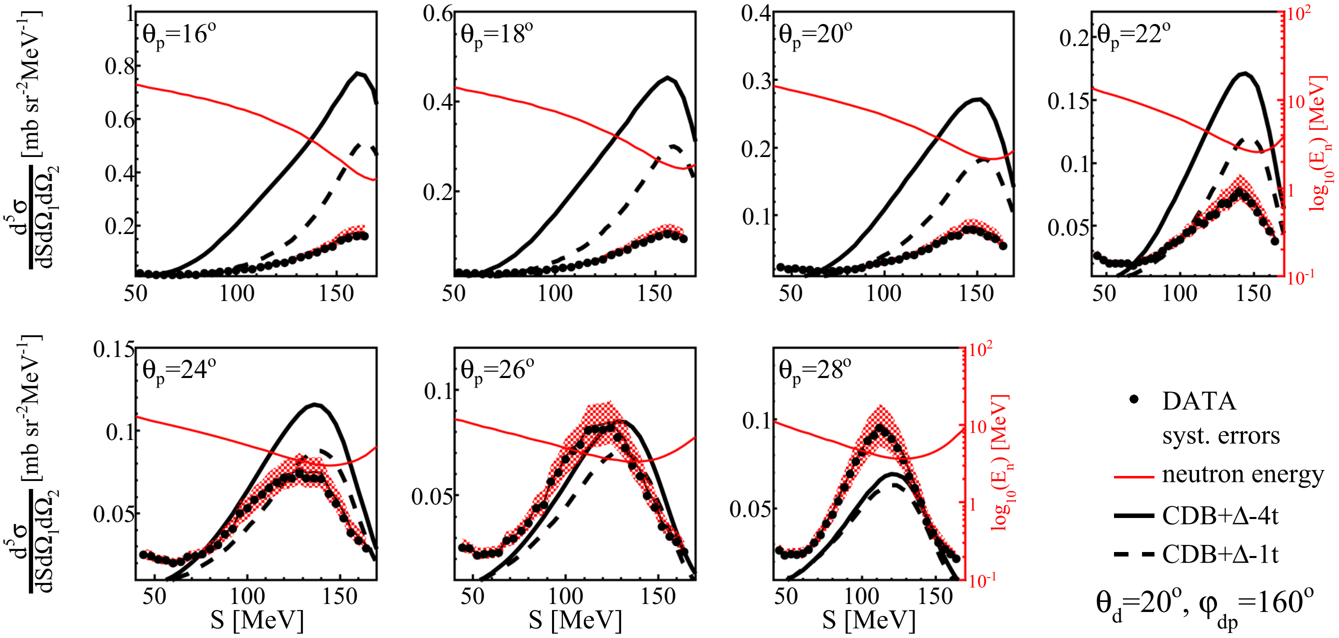

FIG. 26. Same as Fig. 24 but for $\theta_d = 20^\circ$.

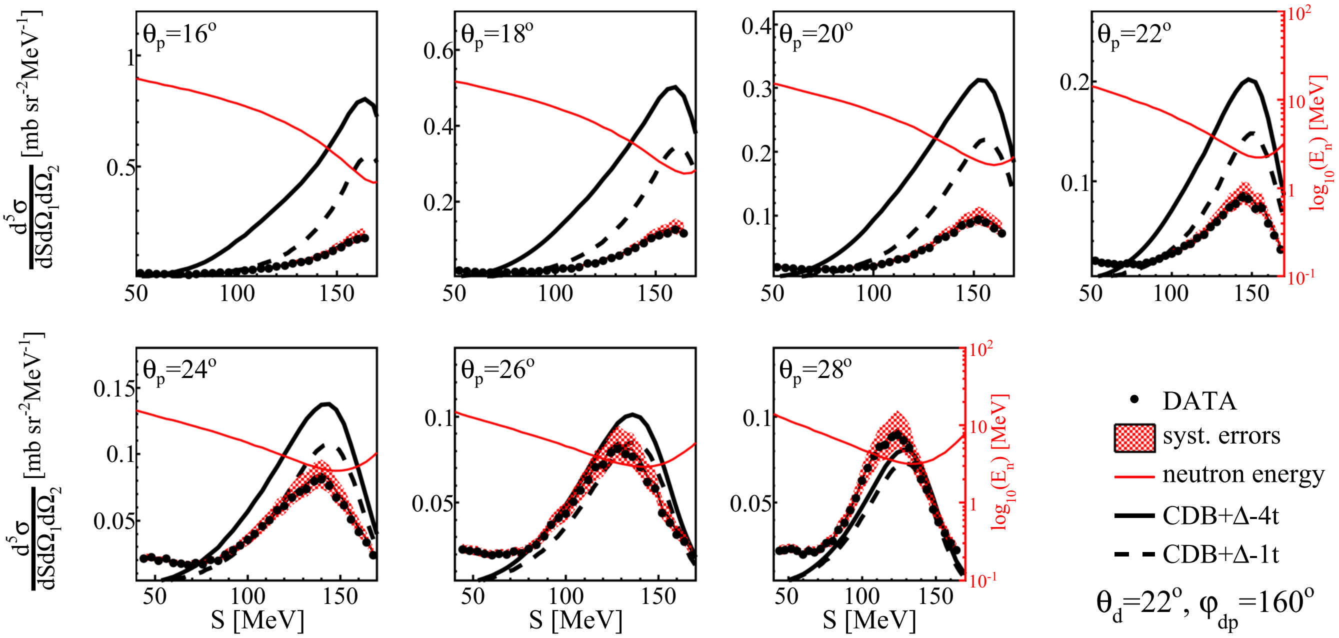

FIG. 27. Same as Fig. 24 but for $\theta_d = 22^\circ$.

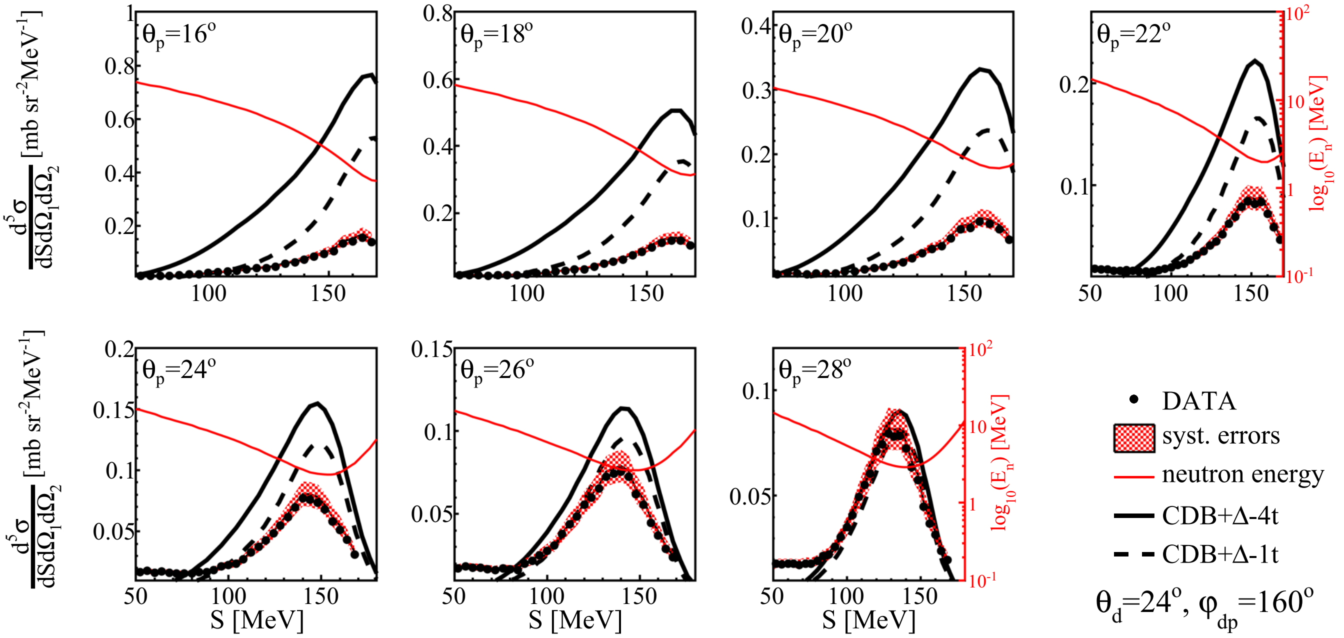

FIG. 28. Same as Fig. 24 but for $\theta_d = 24^\circ$.

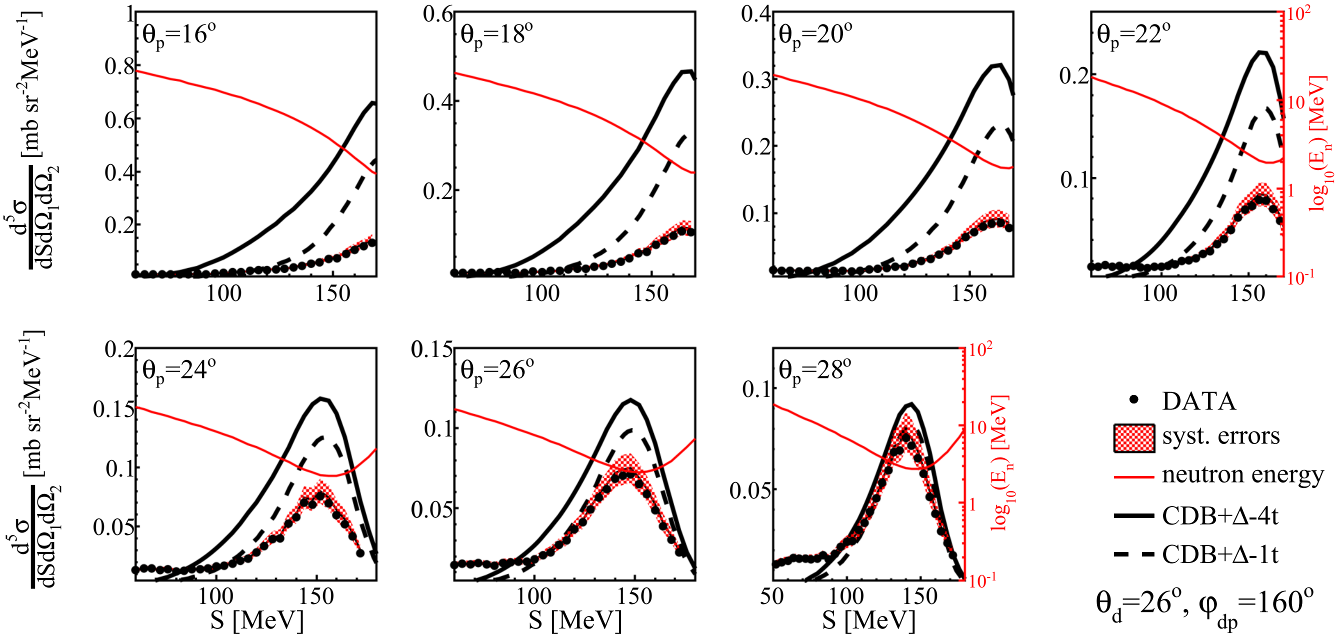

FIG. 29. Same as Fig. 24 but for $\theta_d = 26^\circ$.

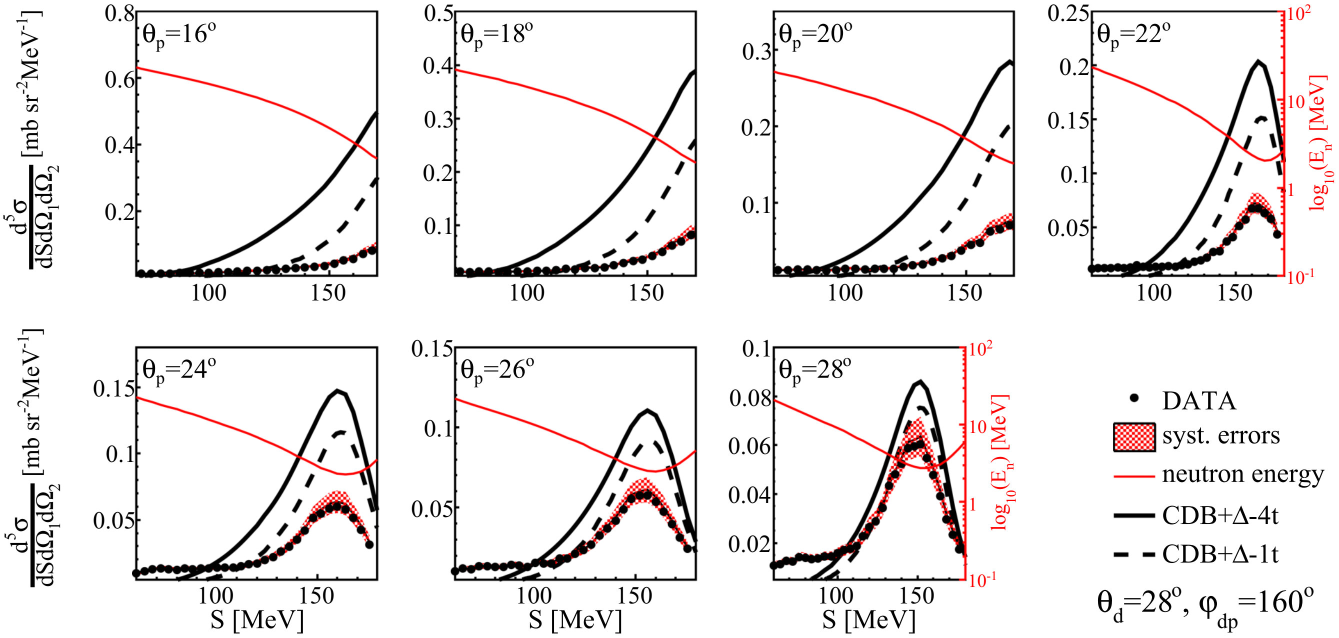

FIG. 30. Same as Fig. 24 but for $\theta_d = 28^\circ$.

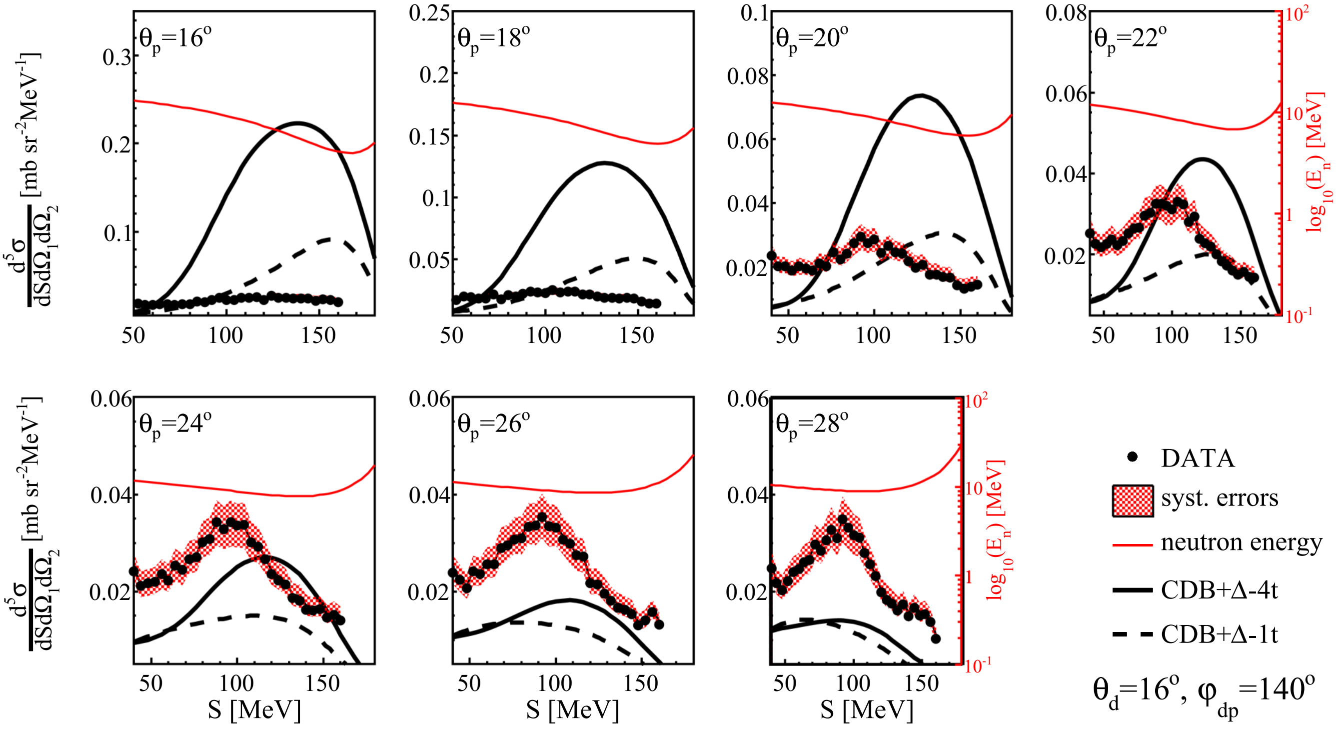

FIG. 31. Differential cross section distributions for the $^2\mathrm{H}(d, dp)n$ reaction obtained for the set of kinematic configurations characterized by $\theta_d = 16^\circ$, $\varphi_{dp} = 140^\circ$, and θ_p as specified in the panels. The dashed black lines represent the one-term (1t) and solid black lines four-term (4t) calculations based on the CD Bonn + Δ potential, as described in the legend. The red (upper gray) line and the scale on the right-hand side present the dependence of the spectator neutron energy (E_n) on the S variable.

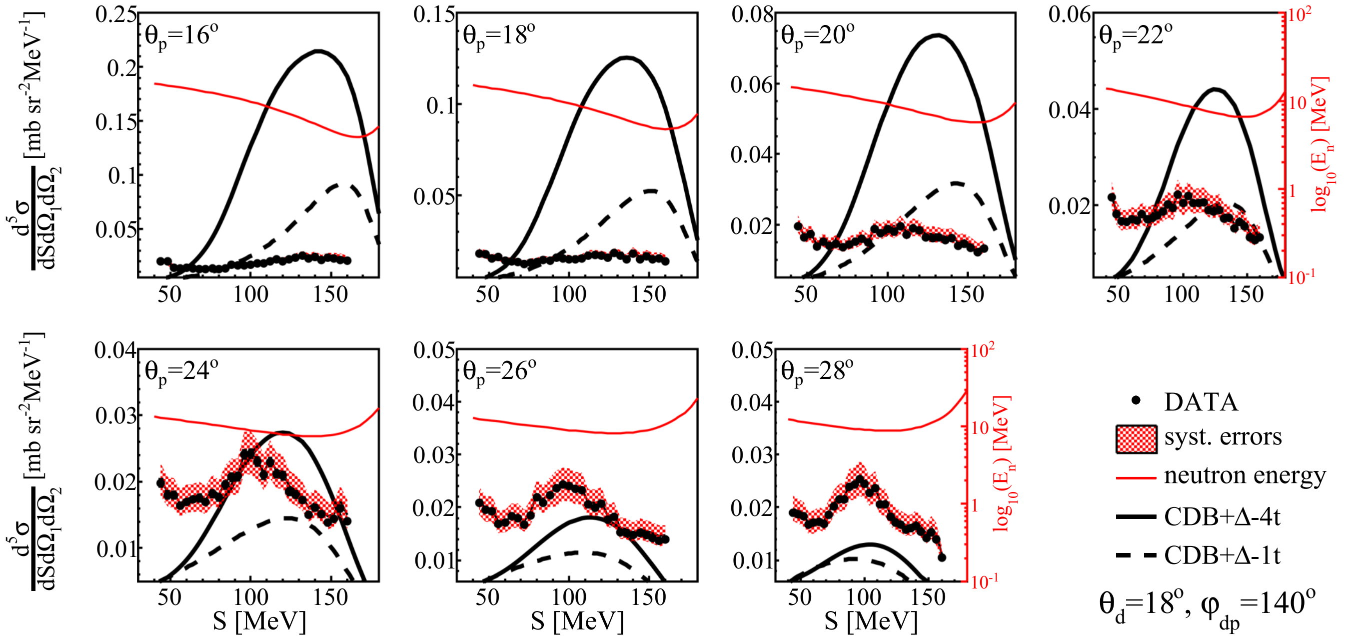

FIG. 32. Same as Fig. 24 but for $\theta_d = 18°$.

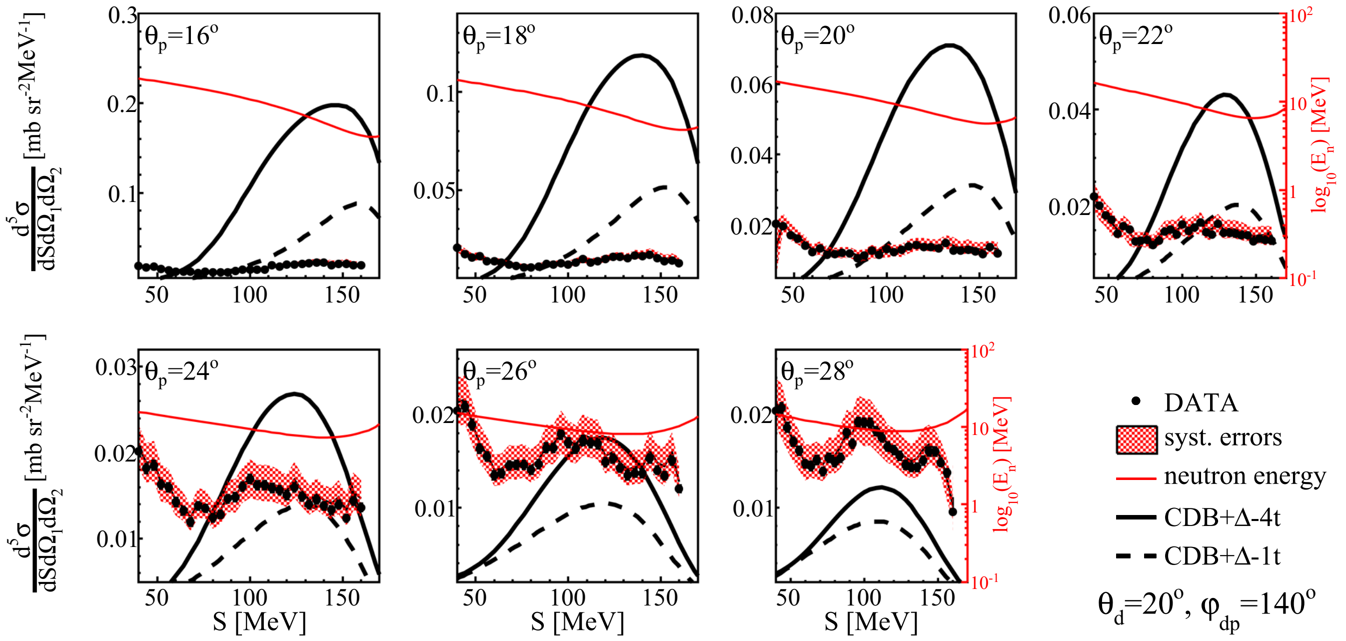

FIG. 33. Same as Fig. 32 but for $\theta_d = 20°$.

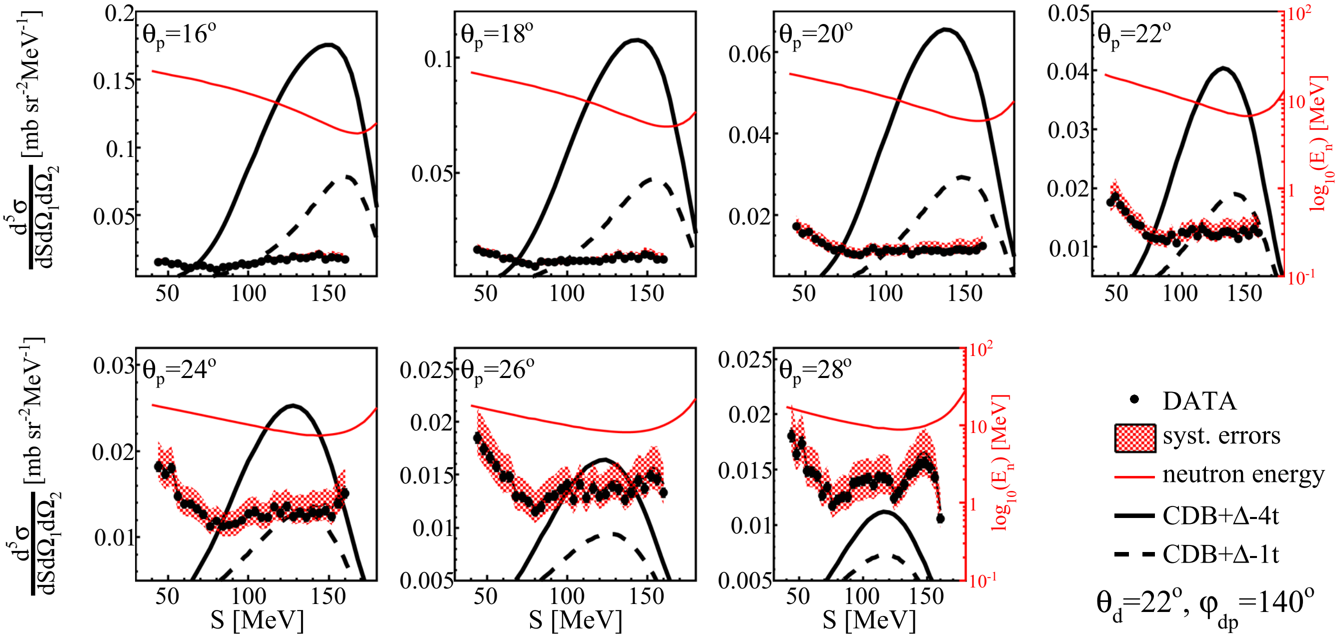

FIG. 34. Same as Fig. 32 but for $\theta_d = 22°$.

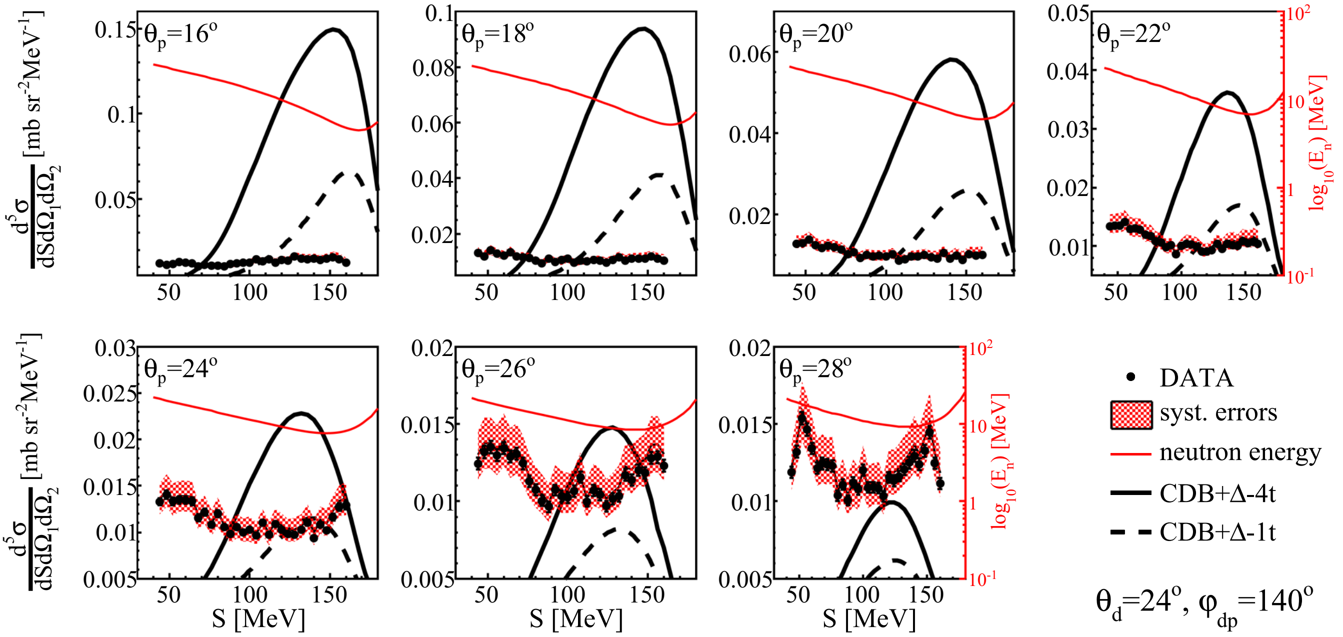

FIG. 35. Same as Fig. 32 but for $\theta_d = 24°$.

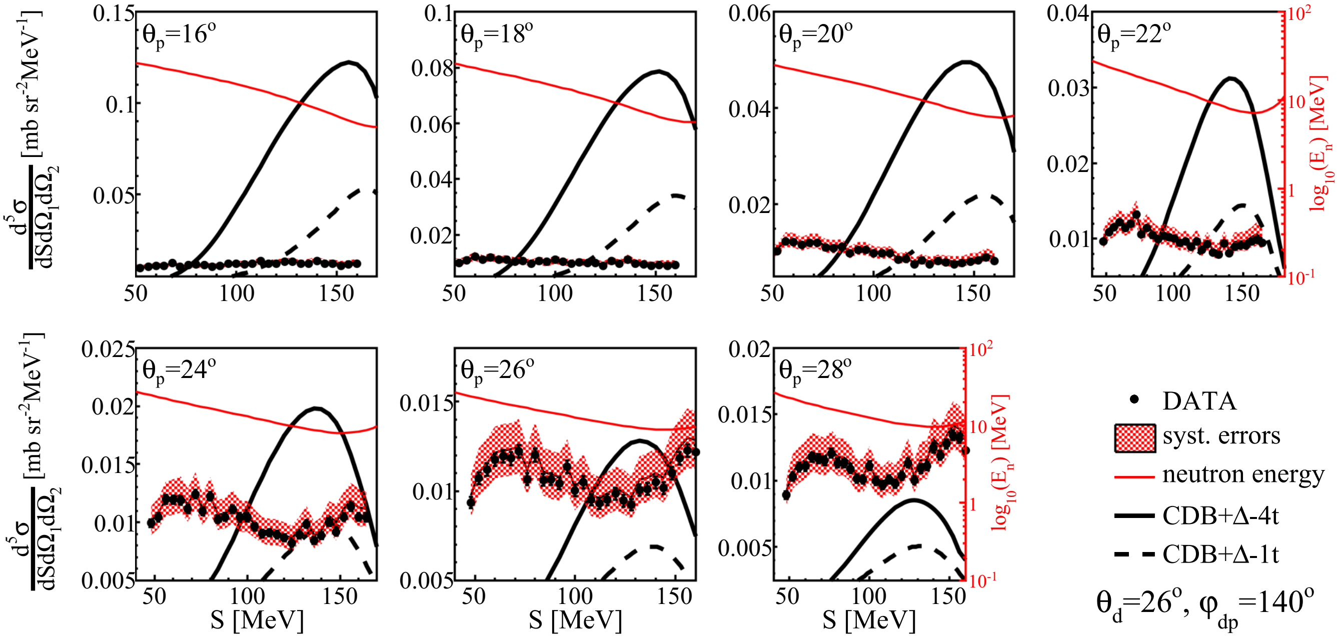

FIG. 36. Same as Fig. 32 but for $\theta_d = 26°$.

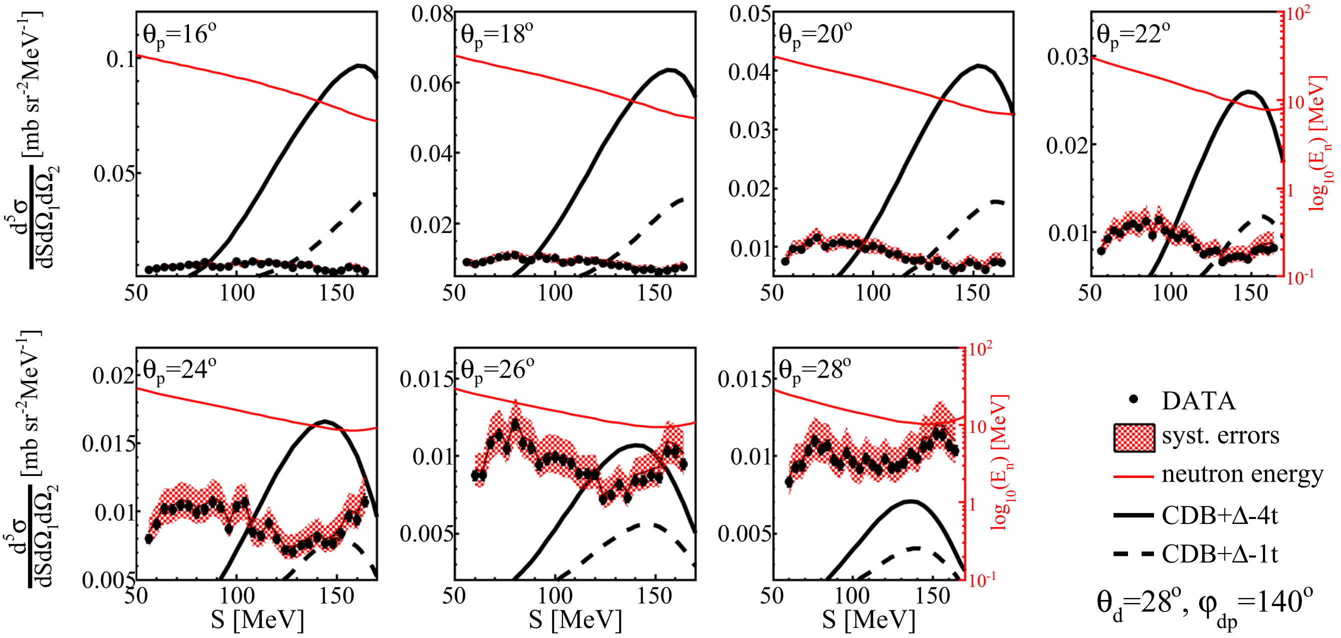

FIG. 37. Same as Fig. 32 but for $\theta_d = 28°$.

[1] K. Sagara *et al.*, Few-Body Syst. **48**, 59 (2010).

[2] N. Kalantar-Nayestanaki *et al.*, Rep. Prog. Phys. **75**, 016301 (2012).

[3] St. Kistryn and E. Stephan, J. Phys. G: Nucl. Part. Phys. **40**, 063101 (2013).

[4] H. Yukawa, Proc. Phys. Math. Soc. Jpn. **17**, 48 (1935).

[5] R. B. Wiringa, V. G. J. Stoks, and R. Schiavilla, Phys. Rev. C **51**, 38 (1995).

[6] R. Machleidt, Phys. Rev. C **63**, 024001 (2001).

[7] V. G. J. Stoks, R. A. M. Klomp, C. P. F. Terheggen, and J. J. deSwart, Phys. Rev. C **49**, 2950 (1994).

[8] L. D. Faddeev, Sov. Phys. JETP **12**, 1014 (1961).

[9] B. S. Pudliner, V. R. Pandharipande, J. Carlson, S. C. Pieper, and R. B. Wiringa, Phys. Rev. C **56**, 1720 (1997).

[10] S. A. Coon and H. K. Han, Few-Body Syst. **30**, 131 (2001).

[11] A. Deltuva, R. Machleidt, and P. U. Sauer, Phys. Rev. C **68**, 024005 (2003).

[12] A. Deltuva, A. C. Fonseca, and P. U. Sauer, Phys. Lett. B **660**, 471 (2008).

[13] D. R. Entem and R. Machleidt, Phys. Rev. C **68**, 041001(R) (2003).

[14] D. R. Entem, R. Machleidt, and Y. Nosyk, Phys. Rev. C **96**, 024004 (2017).

[15] St. Kistryn *et al.*, Phys. Rev. C **68**, 054004 (2003).

[16] St. Kistryn *et al.*, Phys. Rev. C **72**, 044006 (2005).

[17] St. Kistryn *et al.*, Phys. Lett. B **641**, 23 (2006).

[18] I. Ciepał *et al.*, Few-Body Sys. **56**, 665 (2015).

[19] K. Sekiguchi *et al.*, Phys. Rev. C **79**, 054008 (2009).

[20] E. Stephan *et al.*, Phys. Rev. C **82**, 014003 (2010).

[21] M. Eslami-Kalantari *et al.*, Mod. Phys. Lett. A **24**, 839 (2009).

[22] M. Viviani, L. Girlanda, A. Kievsky, and L. E. Marcucci, Phys. Rev. Lett. **111**, 172302 (2013).

[23] R. Lazauskas, Phys. Rev. C **79**, 054007 (2009).

[24] J. Esterline and W. Tornow, Few-Body Sys. **54**, 1323 (2013).

[25] E. Hiyama, R. Lazauskas, J. Carbonell, and M. Kamimura, Phys. Rev. C **93**, 044004 (2016).

[26] A. Kievsky *et al.*, J. Phys. G **35**, 063101 (2008).

[27] R. Lazauskas and J. Carbonell, Phys. Rev. C **70**, 044002 (2004).

[28] A. Deltuva and A. C. Fonseca, Phys. Rev. C **90**, 044002 (2014).

[29] A. Deltuva and A. C. Fonseca, Phys. Lett. B **742**, 285 (2015).

[30] E. O. Alt, P. Grassberger, and W. Sandhas, Phys. Rev. C **1**, 85 (1970).

[31] P. Doleschall, Phys. Rev. C **69**, 054001 (2004).

[32] A. Deltuva and A. C. Fonseca, Phys. Rev. C **87**, 054002 (2013).

[33] A. Deltuva and A. C. Fonseca, Phys. Rev. C **93**, 044001 (2016).

[34] A. Deltuva and A. C. Fonseca, Phys. Rev. C **95**, 024003 (2017).

[35] C. Alderliesten, A. Djaloeis, J. Bojowald, C. Mayer-Boricke, G. Paic, and T. Sawada, Phys. Rev. C **18**, 2001 (1978).

[36] A. Micherdzińska *et al.*, Phys. Rev. C **75**, 054001 (2007).

[37] C. Bailey, Ph.D. thesis, Indiana University, 2009 (unpublished).

[38] A. Ramazani-Moghaddam-Arani *et al.*, Phys. Rev. C **83**, 024002 (2011).

[39] V. Valković *et al.*, Nucl. Phys. A **183**, 126 (1972).

[40] A. A. Cowley *et al.*, Nucl. Phys. A **220**, 429 (1974).

[41] T. Yuasa, H. Nakamura-Yokota, and N. Fujiwara, Prog. Theor. Phys. Suppl. **61**, 161 (1977).

[42] W. Kluge *et al.*, Nucl. Phys. A **302**, 93 (1978).

[43] B. J. Wielinga *et al.*, Nucl. Phys. A **383**, 11 (1982).

[44] L. T. Myers, J. M. Lambert, P. A. Treado, I. Slaus, E. P. Harper, D. W. Devins, and R. G. Allas, Phys. Rev. C **28**, 29 (1983).

[45] G. Bizard *et al.*, Phys. Rev. C **22**, 1632 (1980).

[46] I. Ciepał, J. Kuboś *et al.*, Phys. Rev. C **99**, 014620 (2019).

[47] A. Ramazani-Moghaddam-Arani *et al.*, Phys. Lett. B **725**, 282 (2013).

[48] H. Mardanpour, Ph.D. thesis, University of Groningen, 2008 (unpublished).

[49] E. Stephan, S. Kistryn, A. Biegun *et al.*, Eur. Phys. J. A **49**, 36 (2013).

[50] E. Stephan, S. Kistryn, A. Biegun *et al.*, Eur. Phys. J. A **42**, 13 (2009).

[51] W. Parol *et al.*, Acta Phys. Pol. **45**, 527 (2014).

[52] G. Khatri, Ph.D. thesis, Jagiellonian University, Kraków, 2015 (unpublished).

[53] J. B. Birks, Proc. Phys. Soc. A **64**, 874 (1951).

[54] https://www.crystals.saint-gobain.com/sites/imdf.crystals.com/files/documents/sgc-bc400-404-408-412-416-data-sheet.pdf.

[55] W. Parol *et al.*, EPJ Web Conf. **81**, 06007 (2014).

[56] W. Parol *et al.*, Acta Phys. Pol. B **10**, 149 (2017).

[57] I. Fröhlich, L. Cazon Boado, T. Galatyuk, V. Hejny, R. Holzmann, M. Kagarlis, W. Kuehn, J. G. Messchendorp, V. Metag, M.-A. Pleier, W. Przygoda, B. Ramstein, J. Ritman, P. Salabura, J. Stroth, and M. Sudol, PoS **ACAT2007**, 076 (2007), arXiv:0708.2382 [nucl-ex].

[58] P. Benz *et al.*, Nucl. Phys. B **65**, 158 (1973).

[59] S. K. Sharma, B. Kamys, F. Goldenbaum, and D. Filges, Eur. Phys. J. A **53**, 150 (2017).

[60] A. Ramazani-Moghaddam-Arani *et al.*, EPJ Web Conf. **3**, 04012 (2010).

[61] I. Ciepał *et al.*, Acta Phys. Pol. B **47**, 323 (2016).

[62] K. Sekiguchi *et al.*, JPS Conf. Proc. **23**, 012007 (2018).

[63] H. Mardanpour *et al.*, Phys. Lett. B **687**, 149 (2010).

[64] S. C. Pieper, V. R. Pandharipande, R. B. Wiringa, and J. Carlson, Phys. Rev. C **64**, 014001 (2001).

[65] S. Gandolfi, J. Carlson, and S. Reddy, Phys. Rev. C **85**, 032801(R) (2012).